

ADVANCED FUNCTIONAL MATERIALS

SKIN-INTEGRATED VIBROHAPTIC INTERFACES

Haptic technologies add a sense of touch to visual and auditory cues, as the basis for advanced forms of virtual and augmented reality experiences. In article number 2008805, John A. Rogers, Yei Hwan Jung, and Jae-Hwan Kim present the recent progress in flexible, skin-integrated haptic interfaces that enable rapid, spatio-temporally programmed perceptions of touch, with an emphasis on emerging thin, flexible devices that can be gently laminated onto the skin at any set of locations across the body.

Skin-Integrated Vibrotactile Interfaces for Virtual and Augmented Reality

Yei Hwan Jung, Jae-Hwan Kim, and John A. Rogers*

Haptic technology involves the use of electrical or mechanical means to stimulate afferent nerves or mechanoreceptors in the skin as the basis for creating sensations of physical touch that can qualitatively expand virtual or augmented reality experiences beyond those supported by visual and auditory cues alone. An emerging direction in this field involves the development of platforms that provide spatiotemporal patterns of sensation to the skin across not only the fingertips, but to any and all regions of the body, using thin, skin-like technologies that impose negligible physical burden on the user. This review highlights the biological basis for skin interfaces of this type and the latest advances in haptics in the context of this ambitious goal, including electrotactile and vibrotactile devices that support perceptions of touch in form factors that have potential as skin-integrated interfaces. The content includes a discussion of schemes for integrating these stimulators into programmable arrays, with an emphasis on scalable materials and designs that have the potential to support soft interfaces across large areas of the skin. A concluding section summarizes the potential consequences of successful research efforts in this area, along with key multidisciplinary challenges and associated research opportunities in materials science and engineering.

ematic accelerations could qualitatively expand such experiences to reach a more meaningful level of immersion in a virtual world.^[2,3] Although programmable engagement of the entire somatosensory system may be difficult to achieve, vibrotactile mechanisms appear increasingly capable of generating a sense of virtual touch, not only at the fingertips but potentially across nearly all regions of the body.^[4–11] Controlled patterns of such vibrations have the potential to provide realistic virtual physical interactions based on rapid, interactive control of spatiotemporal patterns of force modulated in magnitude and frequency over large areas at fine resolution.^[12] Efforts to understand the vibratory characteristics of sensorimotor functions of the skin and to develop materials and skin-like systems for vibratory inputs across all regions of the body will lead to profound advances in technologies for VR/AR, with applications that range from virtual social engagements,

1. Introduction

Rapid advances in technologies for virtual reality (VR) and augmented reality (AR) serve as the basis for hyper-realistic, nearly flawless visual and audio simulations of computer-generated environments.^[1] The addition of tactile sensations and kin-

immersive gaming/entertainment experiences and interactive learning, to remote protocols for medical diagnosis, treatment, training, and rehabilitation, to interactive human-machine interfaces.^[13–25]

Existing haptic systems in smartphones, watches, and game controllers, as well as those in emerging modular devices that integrate into garments (i.e., gloves, vests, etc.), rely primarily on actuators that induce vibratory sensations in the skin. A timeline of technology developments in haptic feedback interfaces to remote or virtual objects appears in **Figure 1**. One of the earliest and most widely adopted examples is the gamepad (Figure 1a), as a modality for interacting with objects or characters in a digital environment.^[26–28] Here, vibratory motors provide haptic feedback to the hands as a basic, physical perception for various gaming and entertainment applications. Commercially successful haptic interfaces for VR/AR systems include, as straightforward extensions of the gamepad, handheld controllers for user-friendly engagements with virtual objects (Figure 1b).^[29–31] Systems of this type enable varied modes of control, including grasping, touching, and triggering. Certain extensions of these haptic interfaces for teleoperation take the form of fabrics or wearable frames (i.e., exoskeletons) as gloves or vests, or as devices that mount on the fingertips (Figure 1c), to allow freedom of movement and manipulation, without the need to touch a pad or to hold a controller.^[6,32–39] The engineering approaches for these wearable technologies remain, however, rather primitive, typically based on separate

Dr. Y. H. Jung, J.-H. Kim, Prof. J. A. Rogers
Querrey Simpson Institute for Bioelectronics
Northwestern University
Evanston, IL 60208, USA
E-mail: jrogers@northwestern.edu

Dr. Y. H. Jung
School of Chemical Engineering
Sungkyunkwan University (SKKU)
Suwon 16419, Republic of Korea

Prof. J. A. Rogers
Departments of Materials Science and Engineering
Biomedical Engineering
Neurological Surgery
Chemistry
Mechanical Engineering
Electrical Engineering and Computer Science
Simpson Querrey Institute and Feinberg Medical School
Northwestern University
Evanston, IL 60208, USA

 The ORCID identification number(s) for the author(s) of this article can be found under <https://doi.org/10.1002/adfm.202008805>.

DOI: 10.1002/adfm.202008805

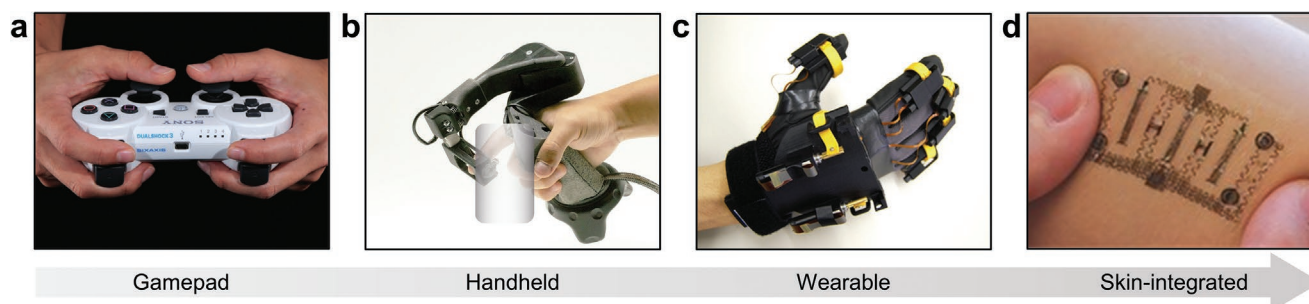


Figure 1. Past, present, and future of haptic technology for virtual and augmented reality. Representative images of haptic interfaces in the form of a) a handheld gamepad, b) a handheld controller, c) an exoskeleton-based or wearable glove, and d) a flexible, skin-integrated epidermal electronic device. Reproduced with permission.^[26] Copyright 2010, John Wiley and Sons. Reproduced with permission.^[29] Copyright 2017, ACM. Reproduced with permission.^[32] Copyright 2007, ACM. Reproduced with permission.^[183] Copyright 2015, Wiley-VCH.

bulk components joined with collections of wires and interfaced to large battery packs.

An important future direction is in haptic interfaces presented by thin, lightweight, devices that can integrate directly as skin-integrated systems onto any or all regions of the body, without constraints or burdens on the user. Such platforms represent conceptual extensions of “epidermal electronics” or “electronic skin” technologies that are rapidly emerging from university laboratories into commercial systems for clinical-grade tracking of physiological status for a broad range of medical applications.^[40–50] Here, soft, biocompatible elastomers combine with stretchable and bendable electronic circuit layouts in hybrid, hard/soft composite structures engineered with guidance from computational models of the mechanics to operate in a physically imperceptible manner, softly interfaced to the surface of the epidermis. A compelling vision is for integration of dense arrays of vibration stimulators into these classes of platforms to deliver rapid and realistic haptic feedback in the form of complex, spatiotemporal patterns of actuation (Figure 1d).^[51] Beyond existing haptic devices that focus almost exclusively on the hands, the ability to deliver fast responding tactile sensations to the skin at any location of the body, without limitation, could serve as the basis for a far more immersive, head-to-toe VR/AR experience, outside of the scope of systems that embed small numbers of actuators into vests, suits, exoskeletons, or tactical gear formats. Advances in functional materials to support mechanical actuation will be critically important for continued development of this field. Successful efforts, taken together with an increasingly broad range of electronic and mechanical design approaches from the field of epidermal electronics, may bypass constraints set by the bulky components, hard-wired interfaces, battery packs, and other features of commercially available technologies that impede mobility and detract from an engaging experience.

This review highlights recent efforts in skin-integrated vibrotactile interface technologies that generate artificial touch sensation through oscillatory excitation. The focus is on emerging research interests in scalable materials and approaches that can support arrays of thin, lightweight stimulators in flexible, skin-conforming platforms capable of mounting across all regions of the body. These technologies are distinct from those that use separate haptic platforms (i.e., tactile displays) that can be contacted with a finger^[52–55] or those exploit bulk, individual devices

that are held in the hand^[30,36] or that mount at discrete locations on the body.^[34] The content includes an overview of past research examples that have potential in this context, as well as some recent work oriented directly at the classes of skin-integrated systems contemplated here. The article begins with a summary of the fundamental aspects of tactile sensation mechanisms of the human skin and its neurophysiology, as important considerations in the design of vibrotactile interfaces. Following sections highlight some of the most promising vibratory stimulator systems, with an emphasis on the functional materials and device designs, their modes of operation, fabrication procedures, electrical/mechanical characteristics, and suitability for use in skin-integrated systems. Of these technologies, electro-tactile stimulators and several types of vibrotactile actuators, such as those based on electromagnetic and piezoelectric effects, successfully apply to haptic interfaces for mimicking touch interactions in VR/AR. Certain of the most advanced examples illustrate how these components can be integrated into thin, flexible platforms with advanced power delivery and wireless control strategies in conformal skin interfaces with consistent/reliable operation in tactile feedback. The article concludes by highlighting opportunities and future directions, with an orientation around research frontiers in functional materials for immersive VR/AR applications uniquely enabled by skin-integrated devices.

2. Toward Artificial Touch Sensations through Mechanical Vibrations

The development of haptic devices requires a deep understanding of the underlying neurophysiological aspects of sensory functions and associated mechanisms of the skin, including effects of spatial variability in the structure of the skin and the nerves across different regions of the body. The units within the skin that are responsible for mechanical sensing, sometimes known as mechanoreceptors, and the nerves that interface them to the brain, known as afferent nerves, reside in the dermis, a layer of skin typically 50–100 μm beneath the surface.^[56,57] Each type of mechanoreceptor responds to different kinds of mechanical stimuli applied to the surface; those adapted to detect vibrations are of particular relevance to the technologies presented in this review. The vibrotactile sensory threshold corresponds to the minimum depth of indentation

at the surface of the skin that is perceptible. By comparison to static deformations, vibratory inputs have far smaller thresholds. The values depend on body location and frequency, extending into the range of 1 mm at 1 Hz, 10 μm at 100 Hz, to 10 nm at 200 Hz.^[58] An additional consideration is that local vibratory deformations can propagate laterally across adjacent regions of the skin, to create unique spatiotemporal propagation patterns that expand the sensory zone beyond the region of direct contact.^[12] The combined effects of these complex sensory features provide an ability to distinguish diverse tactile sensations associated with vibrations, thereby creating many opportunities for the development of materials and devices as vibrohaptic interfaces in skin-integrated, array formats to replicate intricate patterns of touch perception.

2.1. Tactile Receptors and Their Response to Vibrations

Discriminative touch arises from low-threshold mechanoreceptors that interface to rapidly conducting myelinated afferents to mediate tactile sensations in response to mechanical

pressures on and/or distortions of the skin.^[59] Four different mechanoreceptive afferent types exist in skin that is free of hair (glabrous skin): slowly adapting type 1 (SA1), slowly adapting type 2 (SA2), rapidly adapting type 1 (RA1), and rapidly adapting type 2 (RA2). The slowly adapting units (SA1 and SA2) respond continuously to steady deformations, whereas the rapidly adapting units (RA1 and RA2) respond primarily to changes in these deformations. These mechanoreceptors are further categorized by the size of the area of deformed skin, where type 1 units (SA1 and RA1) and type 2 units (SA2 and RA2) support low and high spatial fidelity, respectively. **Figure 2a** presents the four primary mechanoreceptors in human skin: Merkel receptors, Meissner corpuscles, Ruffini endings, and Pacinian corpuscles.^[60] The three major components of the skin are the epidermis (outermost protective layer; ≈ 0.05 mm thick), the dermis (structural support layer beneath the epidermis; 0.6–2.7 mm thick), and the hypodermis (insulating and padding layer beneath the dermis; 0.3–12 mm thick).^[61–63] Located in the basal epidermis, the Merkel receptors (SA1) innervate densely in the skin (≈ 100 afferents per cm^2) to sense points, edges, and curvatures with a receptive field diameter of 2–3 mm.^[64]

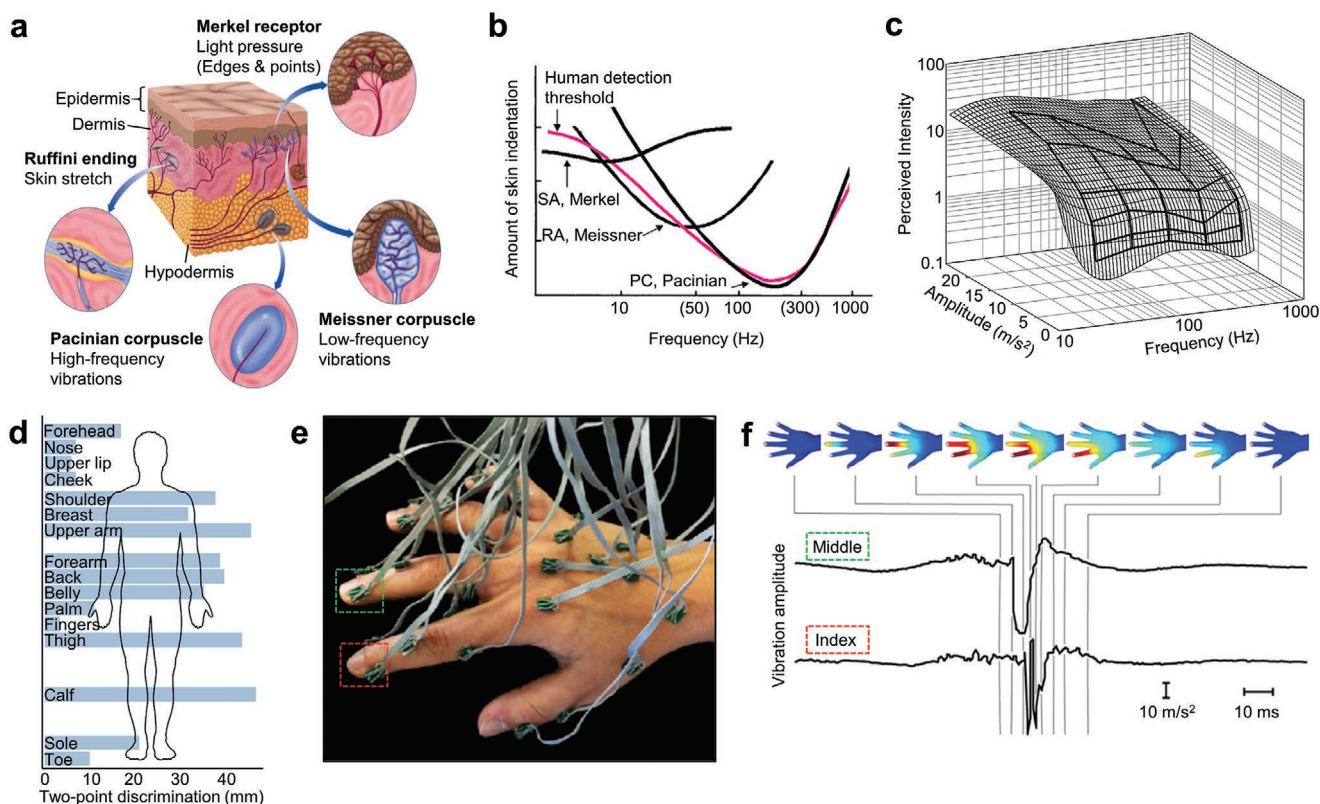


Figure 2. Considerations in the generation of tactile sensations of artificial touch using vibrohaptic interfaces. a) Schematic illustration of the four primary mechanoreceptors in human skin. Reproduced with permission.^[60] Copyright 2013, Cengage Learning. b) Graphs of thresholds for detection of vibrotactile stimulation at different frequencies. Reproduced with permission.^[69] Copyright 2007, Springer Nature. c) 3D representation of perceived intensities of vibrotactile sensations (solid lines) as a function vibration amplitude (i.e., acceleration) and frequency. The graph also shows a surface obtained using a nonlinear regression model. Reproduced with permission.^[73] Copyright 2010, Massachusetts Institute of Technology. d) Results of two-point discrimination tests on different parts of the human body. Reproduced with permission.^[78] Copyright 2018, Elsevier. e) Photograph of an array of 30 accelerometers attached to various locations across the hand for evaluating spatiotemporal patterns of vibrations during touch interactions. f) Illustration of the spatiotemporal distribution of vibration intensity generated by tapping the index and middle fingers on a steel plate (top). The time course of evolution of acceleration (y axis) at locations on the distal phalangeal area of the index and middle finger (bottom). Reproduced with permission.^[12] Copyright 2016, National Academy of Sciences.

Individual Merkel receptors resolve spatial detail of 0.5 mm and convey information about static stimuli with indentation depths of at least 1.5 mm. Meissner corpuscles (RA1), also in the basal epidermis, respond to fine touch, as well as low-frequency vibrations (10–50 Hz) with skin indentations of less than 10 μm .^[65] These receptors respond to stimuli within a receptive field of between 3 and 5 mm in diameter. Ruffini endings (SA2) reside in the superficial dermis. With a receptive field of 10–15 mm in diameter, these endings signal stretching of the skin effectively. Their sensitivities to stretch and to indentation are 2–4 times more and 6 times less than those of Merkel receptors, respectively. Pacinian corpuscles (RA2), located in the deep part of the dermis or in the hypodermis, detect transient pressures, and high-frequency vibrations with sensitivities of less than 10 nm at 200 Hz. Their extreme sensitivity and their deep location lead to receptive fields of larger than 20 mm.^[58] By comparison to glabrous skin, hair bearing regions contain proportionally fewer afferent nerves and Meissner corpuscles. Here, rapidly adapting mechanoreceptors associated with hair cells, and low-threshold, slowly-conducting, unmyelinated C-tactile (CT) afferents serve as the basis for touch sensation. These CT afferents are also responsible for the affective properties of touch, such as positive and negative emotions.^[59,66]

Each of these four mechanoreceptors (Figure 2a), except for the Ruffini endings, detect vibrations at specific ranges of frequencies. During the perception process, a sinusoidal vibration introduced at the surface of the skin develops into action potentials that transmit through the receptors. Each action potential signal corresponds to a single cycle of oscillation. The amplitudes of the vibratory deformations determine the total number of activated nerve afferents. A series of such action potentials from different receptor activations, followed by synchronous and repetitive discharge, forms the basis of a perception of vibration.^[67] In general, Merkel receptors detect very low frequency (below ≈ 15 Hz) vibrations, Meissner corpuscles detect low frequency (2–100 Hz) vibrations, and Pacinian corpuscles detect vibrations that reach the highest perceptible frequencies (40–500 Hz).^[68] The sensitivity thresholds for vibration depend on the size and frequency of skin indentation; the values depend on receptor type (Figure 2b).^[69] The thresholds measured from human subjects, summarized in Figure 2b, indicate that the highest sensitivity to vibrations occurs in a frequency range from 200 to 250 Hz. The median thresholds for Merkel receptors, Meissner corpuscles, and Pacinian corpuscles are 56.5, 13.8, and 9.2 μm , respectively.^[7]

Based on feedback from subjects stimulated with multiple different waveforms over the frequencies of 0–300 Hz, bands of sensitivity fall into three distinctive perceptual qualities: slow motion (up to ≈ 6 Hz), fluttering motion (≈ 10 –70 Hz), and smooth vibration (above ≈ 150 Hz).^[70] Different psychophysical experiments also reveal that a stimulus in the range of 5–40 Hz feels like a light flutter of the skin that can be localized accurately.^[71] This sensation changes into a vibratory hum as the frequency increases to values between 60 and 80 Hz.^[72]

In addition, psychophysical studies of perceived intensities of sensations due to vibrations as a function of frequency for various fixed amplitudes (i.e., accelerations) reveal the key effects. The 3D plot in Figure 2c represents the relationship between perceived intensity, amplitude and frequency, based on reports of 11 participants for 30 conditions of

sinusoidal vibrotactile stimuli transmitted to the hand generated from a mechanical shaker.^[73] Specifically, the participants grasp a mobile device designed to mimic vibrotactile feedback mechanisms available in mobile phones. Here, a zero perceived intensity represents a detection threshold, the smallest signal that is perceived. The perceived intensity increases monotonically with acceleration at a fixed frequency and decreases with frequency at a fixed acceleration. In terms of vibrational displacement, a plot that represents displacement against frequency at a fixed perceived intensity follows the U-shape curve of Figure 2b, as the functional relationship of perceived intensity with stimulus frequency depends on the detection threshold.^[74] This result suggests that generating vibrations with a similar perceptual magnitude requires greater accelerations at higher frequencies.^[75]

2.2. Tactile Sensitivity across the Human Body

The nature of spatial variations of the perception of touch across the body are also important to consider. Receptors tend to be densely arrayed in the face and hands, with comparatively sparse distributions across areas of the back and thighs. The number of receptors determines the sensitivity of the skin, not only by the magnitudes of the deformations but also in terms of their spatial details. The two-point discrimination test records the smallest distance between two sharp points that are perceived as distinct stimuli.^[76,77] This test represents a standard method for determining the spatial resolution of the sensitivity. Results from such measurements performed on different parts of the body (Figure 2d) reveal that skin associated with the face and hands offer the finest resolution, to scales of 2–4 mm on the fingertips.^[78] By contrast, regions such as the upper arm, thigh, and calf support resolution that is ten times more coarse, in the range of ≈ 40 mm.

Psychophysical tests define the tactile sensitivity based on patient reports of sensation upon pressing skin using monofilaments. The contact force required to stimulate receptors in the forehead and palm must exceed 0.6 mN.^[79] On the thigh and shin, this force increases by more than ten times (10 mN). Such differences relate directly to the spatial distribution of the mechanoreceptors. Out of roughly 45 624 mechanoreceptors across the entire body, ≈ 18 675 mechanoreceptors reside on one hand, which comprises of only 1.2% of the total skin area.^[80] In comparison, only 2105 and 443 mechanoreceptors reside on the back (13.9% skin area) and thigh (9.2% skin area), respectively. The vibrotactile sensory thresholds at 200 Hz for the hand, back, and thigh are 0.07, 1.4, and 1.8 μm , respectively.^[81] The reaction time relates to the distance between the stimulated site and the brain, which determines the neural transfer times. The temporal resolution at different skin sites ranges between 5 and 25 ms.^[82]

2.3. Spatiotemporal Patterns of Vibrations across the Skin

As suggested previously, complex spatiotemporal patterns of propagating deformations during physical interactions with the skin form important additional aspects of tactile sensation. Specifically, touching an object not only excites the receptors at the region of direct contact, but also across adjacent areas separated

in distance by as much as a few centimeters, as distributed vibratory and static disturbances through the tissues of the skin.^[83–85] Different modes of interactions, such as tapping or sliding against a metal or fabric surface, induce different spatiotemporal patterns. Detailed studies that exploit arrays of accelerometers attached at different locations of the hand capture these effects as dynamic and spatial vibrations during various modes of skin interactions (Figure 2e).^[12] Videos of color maps of averaged acceleration magnitudes yield visual representations of the spatial and temporal patterns of vibration intensity for different interaction modes. The results of measurements for a variety of manual interactions reveal that vibration intensities yield interaction-dependent distributions of deformations that peak/fade rapidly within a few milliseconds. As might be expected, vibration amplitudes at the region of skin-object contact are larger for interactions with hard objects (e.g., 4.7 m s^{-2} for steel) compared to those with soft objects (e.g., 2.4 m s^{-2} for fabric). Moreover, tapping causes more broadly distributed patterns of vibration compared to those for sliding contact. Likewise, increasing the force of the contacts increases the spatial extent of these patterns. As a specific example, tapping a surface with the fingertips leads to deformations that propagate across the dorsal surface and dissipate at the wrist, within 20–30 ms of the instant of contact.

Figure 2f shows an example of a measured spatiotemporal distribution of vibration intensity and the corresponding time course of evolution of acceleration for the case of tapping index and middle fingertips against a steel plate. The largest amplitudes occur in a frequency band of 10–100 Hz, in such cases. Distinct patterns of vibration energy that arise from hand gestures associated with indirect tapping and grasping demonstrate the importance of the frequency content of the propagated energy. Energy appears mainly in a frequency band of 200–400 Hz for indirect tapping, such as tapping a surface with a stylus. Grasping a soft ball induces little vibrational energy above 10 Hz.

These and other findings establish important considerations in the development of haptic interfaces. Specifically, the complex, sophisticated nature of the mechanoreceptor system indicates that achieving a realistic sense of touch with such an interface technology requires thoughtful consideration and implementation of the actuators, their spatial distribution, and the temporal characteristics of their operation. The broad frequency range that characterizes the responses of mechanoreceptors in the skin, and in particular their high sensitivity to vibratory inputs, creates significant opportunities in the development of vibrohaptic feedback as a means to mimic the perception of touch with high levels of richness and complexity. Manipulating the frequency and amplitude of vibrations can produce a wide range of tactile sensations. The frequency dependence of the threshold for sensation in Figure 2b suggests that frequencies below 100 Hz require actuators with large amplitudes to achieve practical levels of perception, sometimes defined by magnitudes that are 10–20 dB above threshold compared to receptors detecting high frequency vibrations.

These and related considerations must also account for the distribution of the afferent nerves and mechanoreceptors across the body. In general, skin regions that have high thresholds also have low spatial and temporal sensitivities, and in such cases, haptic interfaces can be achieved with sparse arrays of powerful actuators. When operated in a coordinated fashion,

such arrays can also reproduce spatiotemporal patterns similar to those observed in the propagation studies described above, for realistic artificial touch. An ultimate solution in the context of VR/AR systems adheres to the vision described previously, of technologies in the form of thin, lightweight flexible arrays, gently interfaced to the soft, curved surfaces of the skin, with wireless, real-time programmability. Recent advances in materials science, mechanical engineering and electrical engineering suggest that such systems are increasingly within reach. The following sections highlight some of the most promising directions in this rapidly growing area of interdisciplinary research.

3. Materials and Designs for Haptic Stimulators

The most well-explored strategies for creating vibrohaptic sensations through physical interfaces to the skin fall into two categories. The first relies on physical forces delivered by functional materials to the mechanoreceptors through electrical, magnetic, pneumatic, hydraulic, piezoelectric, or other effects, in methods known collectively as vibrotactile stimulation.^[7] The second exploits currents injected from skin-contacting electrodes to underlying afferent nerves, in a scheme referred to as electro-tactile stimulation.^[86] Figure 3 shows representative images of promising mechanisms of these types as skin-integrated vibrohaptic interface systems. Each technique has strengths and weaknesses. For example, electro-tactile stimulation has the advantage of simplicity and immediate ability to scale to arrays in platforms that can adopt thin, stretchable form factors to facilitate integration with the skin. A drawback is that such approaches require careful selection of the skin-contacting electrode materials and precise control over the injected currents to allow safe, controlled operation.

Vibrotactile actuators of various types avoid these challenges through the delivery of mechanical stimuli using biocompatible materials at the skin interface in designs that guarantee safe, pain-free operation. The main challenge in electromagnetic devices for such purposes is that achieving sufficient forces and displacements typically demand complex designs, bulky components, and poor power efficiencies. Alternative schemes such as those based on pneumatic effects or functional materials allow for miniaturized dimensions and scalable fabrication, but they also demand high voltages and/or power for operation, often with requirements for externalized hardware for pumping, as an example. The following sections summarize the latest advances in these technologies, including those that have some promise but have not yet been explored in the types of large, thin, and skin-integrated platforms envisioned here.

3.1. Electrotactile Stimulators

An electrical current injected through an electrode pair attached to the skin generates a potential gradient that depolarizes the afferent nerves under the electrode that serves as the cathode. The nerves activate above a certain threshold potential. Therapeutic electrical nerve stimulation, reflex stimulation, muscle activation, and defibrillation are examples of applications that use this mechanism. Due primarily to its simplicity, electro-tactile stimulation is one of the most widely explored approaches

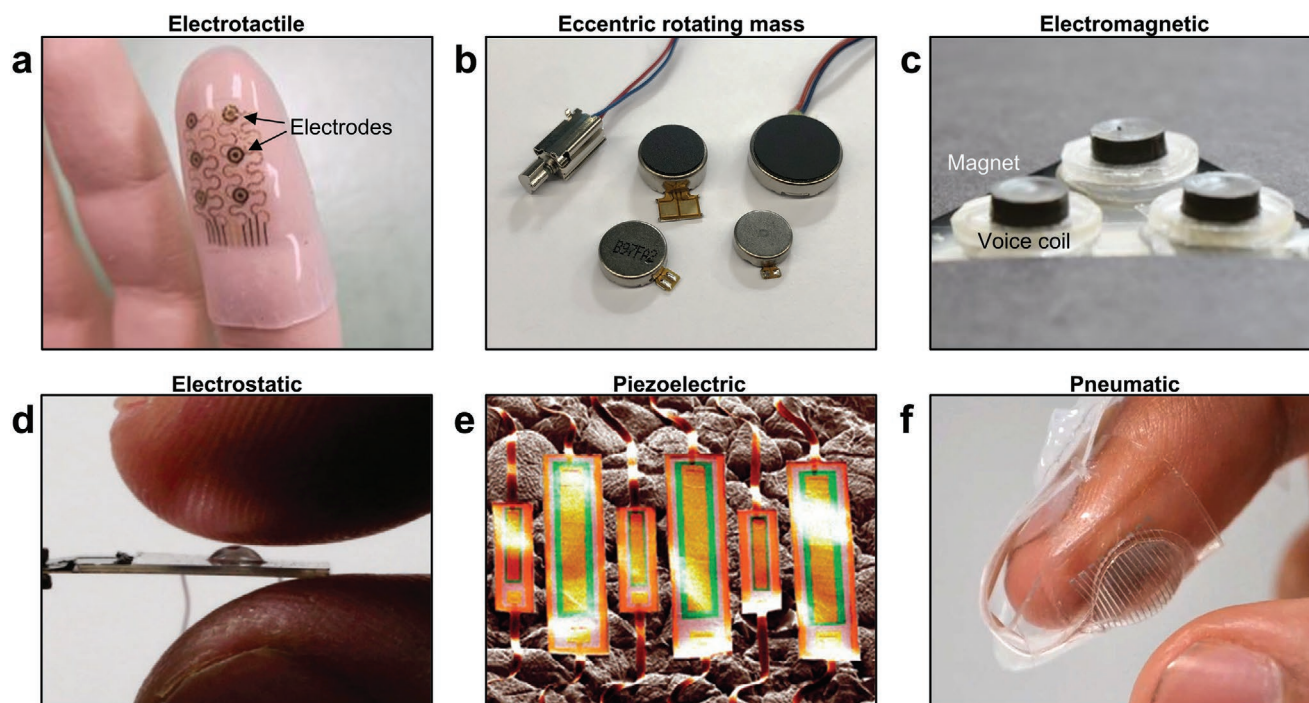


Figure 3. Materials and device structures for vibrohaptic interfaces. a) Photograph of an electro-tactile stimulator on a fingertip. b) Photograph of several commercial eccentric rotating mass actuators. c) Photograph of a voice coil-based electromagnetic actuator. Reproduced with permission.^[106] Copyright 2018, Wiley-VCH. d) Photograph of a hydraulically amplified tassel actuator in actuated states, with the finger for scale. Reproduced with permission.^[133] Copyright 2020, Wiley-VCH. e) Scanning electron microscope image of an array of ultrathin piezoelectric actuators and sensors laminated onto a replica of human skin. Reproduced with permission.^[162] Copyright 2015, Springer Nature. f) Photograph of a wearable pneumatic vibrotactile actuator mounted on a fingertip. Reproduced with permission. Copyright, Reconfigurable Robotics Lab, EPFL.

for inducing tactile sensations.^[87–89] Choices of electrical stimulation parameters and electrode geometries determine the intensities and patterns of sensation, as the basis for programmable control. Applying appropriate electrical waveforms to the electrodes activates afferent nerves as the source of a sense of vibration in a way that largely bypasses the role of the mechanoreceptors. Typical electrical current density levels applied to the skin range from 0.1 to 10 mA cm⁻² at corresponding voltages of between 30 and 50 V using electrodes that have lateral dimensions in the range of 2–40 mm.^[90–93]

Systems in arrayed geometries can be constructed with thicknesses typically far less than 1 mm, in physical forms that can approach those of the skin itself. The selection of electrode sizes depends on the size of the targeted skin area and on the thickness of the underlying fat layer. For example, the effectiveness of electrical stimulation with small electrodes decreases as the thickness of underlying fat layer increases, due to the large current spread. The current densities required for operation span a wide range, due to the strong dependence of perceptual threshold levels on electrode characteristics and locations of stimulation. Inhomogeneities in the skin and across the electrodes and their skin interfaces greatly influence current density distribution, affecting stimulation efficiency and comfort differently across different parts of the skin. Section 4.1.1 highlights these issues in detail.

Popular electrode materials include mixed layers of conventional, skin-compatible metals such as gold, stainless steel, and platinum^[7,94] as well as soft conductive hydrogels and

carbon impregnated elastomers.^[90–92,95,96] In some cases, layers of poly(3,4-ethylenedioxythiophene) polystyrene sulfonate (PEDOT:PSS) or silver/silver chloride (Ag/AgCl) serve to control the overall resistivity of the electrodes and the contact impedance to the skin.^[97,98] These and other electrode materials are often derived from those used in electrophysiological recordings, such as electrocardiograms, electromyograms (EMG) and electroencephalograms, due to a similar set of considerations and requirements.

An additional aspect in the selection of electrode materials depends on the trade-off between the homogeneity of current distribution and the resistivity of the electrodes. Low resistivity can result in a less homogeneous current distribution, while high values can lead to high voltages at the stimulation electrodes. A resistivity above the value of the skin ($\rho_{\text{electrode}} > 700 \Omega \text{ m}$) typically results in an acceptable current distribution.

Traditional electro-tactile stimulators include a pair of electrodes, one as an active interface and another as a reference, typically with rectangular or circular shapes and lateral dimensions of a few or a few tens of millimeters. Many reported schemes use hydrogels coated on top of electrodes of Ag, AgCl, and/or carbon. A representative case uses a skin-contacting, electrically conductive hydrogel with relatively low peel strength for easy removability from the skin, a second hydrogel layer with low resistivity for even current distribution, and a conductive fabric-based substrate with connector leads. An alternative layout involves a concentric geometry in which a ring-shaped reference electrode surrounds a central, disc-shaped active electrode in a

coaxial configuration to localize the induced sensation and minimize interference with measurements of EMG or other electrophysiological signals for control or feedback.^[95] A commercial electrode structure in this type of concentric format (40 mm in diameter; Spes Medica) has an active electrode diameter of 10 mm and reference electrode ring outer diameter of 30 mm, with a 5 mm separation in between.^[99] Arrays of microelectrodes for electrotactile stimulation can support high spatial densities, as patterned metal films on thin sheets of plastic or, preferably, elastomeric substrates to facilitate mechanically compliant integration with skin. Figure 3a shows an electrotactile stimulator designed for the fingertips using stretchable, filamentary serpentine interconnects to ensure low modulus, skin-like properties.

A key concern in electrotactile stimulators arises from the need to maintain sufficient levels of current injection to elicit robust sensations, but at values below those that create uncomfortable or even painful responses. The challenge is that the electrical impedance at the skin interface can vary widely between individuals and even across the body of a given subject. Changes can also occur over time due to sweating, fluctuations in the hydration level of the skin and other factors. Engineering solutions therefore require careful attention to the hardware designs, specifically to electronic systems that provide feedback control over the stimulation parameters and to materials that support robust, skin-integrated electrical interfaces with consistently low impedance. Section 4.1 discusses some features of the most advanced skin-integrated electrotactile stimulators in detail.

3.2. Vibrotactile Stimulators

As mentioned previously, mechanical stimulation of the skin avoids many of the challenges associated with electrical approaches. Several different materials and device designs for this type of vibrotactile interface have promise for future haptic systems. The following describes the main classes of these technologies, their operational mechanisms and key attributes.

3.2.1. Electromagnetic Actuators

Electromagnetic actuators that rely on Lorentz forces, such as eccentric rotating mass actuators (ERM), are ubiquitous in mobile electronic devices and gaming controllers.^[100,101] ERM actuators (Figure 3b) are direct current (DC) motors that include an off-center mass attached to a rotation shaft, in designs commonly referred to as “eccentric.” Rapid rotations lead to vibratory actuation generated by uneven centripetal forces, typically resulting in side-to-side motions. Commercially available ERM actuators include those in small coin cell packages (7 mm in diameter, 2 mm in thickness, 0.6 g in weight; Jinlong Machinery) or cylinder-like form factors (10.8 mm in length, 3.0 mm in height, 0.9 g in weight; Jinlong Machinery), with simple, cost-effective designs and capabilities for generating strong vibrational forces.^[102] Coin cell-type designs are attractive for haptics because the housing seals all moving parts to facilitate physical interfaces with the skin in convenient geometries. Such devices also often include a commutation circuit board built around a shaft in the center,

a rotor with two voice coils and an eccentric mass that rests on the shaft through a center bearing, with a disk-type magnet that attaches to the motor chassis. At the underside of the rotor, two metal brushes that connect to the voice coils establish contacts to the commutation circuit, in which a current generates a magnetic field in the coils. This field interacts with the flux of the magnet and, in turn, moves the rotor, allowing the metal brushes to alternate the direction of field.

All commercially available ERM actuators utilize powerful neodymium-based (i.e., NdFeB) magnets, a rare-earth alloy that can reduce power consumption by half compared to otherwise similar designs that incorporate alnico (i.e., alloy of Al, Ni, and Co) or ferrite (i.e., Fe₃O₄) magnets. The typical operating voltages range from 1.5 to 3.3 V, and power consumption levels range from ≈60 to 200 mW, depending on vibration strength. The speed of the motor increases with supplied voltage, to increase the frequency of vibration by a corresponding amount.

The inductive and resistive characteristics of the motors average a supplied pulse-width modulation (PWM) signal into a DC voltage that is proportional to the duty cycle. Precise control of the vibration using this PWM scheme can be achieved easily with standard microcontrollers. The main drawbacks are in intrinsically slow transition times between steady and moving states (≈50 ms) and in limitations in control that follow from interrelationships between the frequency and amplitude of the response. The first issue can be addressed, to a certain extent, by using an initial overdrive voltage to overcome the inertia of the eccentric mass and to quickly start the rotation before a transition to the rated voltage.^[103,104]

Vibration strengths of ERM actuators vary according to size and other properties, and are measured as maximum accelerations (units of Gs, the acceleration from gravity; 9.81 m s⁻²) for a 100 g mass load.^[105] For actuators within lateral dimensions of ≈1 cm, the vibration strengths for coin cell-type ERMs range from 0.35 G (6.0 mm in diameter, 1.8 mm in thickness) to 3.0 G (12 mm in diameter, 3.4 mm in thickness). Values for cylinder-like ERMs range from 0.25 (9.4 mm in length, 4.0 mm in height) to 3.0 G (16.3 mm in length, 6.2 mm in height) at input DC voltages of 3.3 V.

Enhanced responsiveness and power efficiency can be achieved with voice coil-based electromagnetic actuators and linear resonance actuators (LRA).^[106–108] These devices (Figure 3c) rely on an electrical current that passes through a loop of wires to induce a magnetic field that exerts actuation on an aligned magnetic material via a Lorentz force. An alternating current (AC) drives the voice coil to produce motions of the magnet, which also acts as a moving mass. Specifically, current through the coil generates a magnetic field, which interacts with the moving magnet to produce an oscillating force across the vertical axis. An additional spring connects the moving mass to the voice coil, creating a perceptible vibration force with low power consumption when the voice coil operates near the resonant frequency of the spring.

Most LRAs operate efficiently only within a narrow band (±2 Hz) around the resonant frequency.^[109,110] A driver integrated circuit (IC) can automatically track this resonance and adjust to achieve maximum efficiency. The rapid response of the moving magnet upon application of a current yields start times (≈30 ms) that are typically shorter than those for an ERM

actuator (≈ 50 ms).^[110] The temporal resolution of the skin, which lies between 5 and 25 ms depending on location, is an important consideration in the design of haptic actuators that can produce sharp and crisp sensory effects. In an LRA, the stop time can be long (≈ 300 ms), due to the stored kinetic and potential energy in the system during actuation. Control systems that integrate active braking functions can improve this aspect of the performance by applying phase-shifted AC signals to generate forces to oppose continued oscillation. As with commercially available ERMs, LRA devices can interfere magnetically with nearby electronics. Additional control systems can minimize such effects. The associated requirements, however, lead to complex operation schemes and specialized drivers.

Nevertheless, LRAs are high-performance and reliable alternatives to ERMs, due mainly to improved response characteristics and efficient spring mechanisms. Coin-cell-type LRAs can generate vibrational strengths in the range of 0.7 G (6.0 mm in diameter, 1.8 mm in thickness) to 1.9 G (12 mm in diameter, 3.7 mm in thickness), at AC voltages between 1.2 and 2.0 V. Comparable LRA devices (12 mm in diameter, 3.4 mm in thickness) consume $\approx 45\%$ of the power required for otherwise similar ERMs (10 mm in diameter, 3.6 mm in thickness) for operation at the tactile threshold (minimal detectable activation levels), at different frequencies (175 Hz for ERM and 69 Hz for LRA).^[111,112]

An additional consideration is that both types of devices can be relatively heavy and bulky because they typically rely on conventional materials, such as stainless steel, neodymium, and copper, for the mass elements, permanent magnets, and coils, respectively. For example, the weight of a small coin cell type ERM or LRA device (2.5–4 mm in thickness, 9–10 mm in diameter) is in the range of 1–2 g. The scalability for reduced sizes and arrayed layouts is limited by manual assembly processes for the constituent components. Alternative materials and device designs may address these drawbacks, as described in the context of electromagnetic vibrotactile actuators for skin-integrated haptic interfaces in Section 4.2.

3.2.2. Electroactive Polymer Actuators

Functional materials that transform electrical energy directly into mechanical vibrations without moving parts avoid the bulk and mechanical complexity of electromagnetic actuators, and they provide straightforward paths to integration into large-scale arrays. Electroactive polymers (EAP) are materials that undergo a dimensional change in response to an applied electric field and/or generate an electrical polarization in response to an applied mechanical stress.^[113–116] These materials appear in a wide range of mechanical sensors and actuators for industrial, medical, consumer, and musical applications.^[117,118] Actuators capable of producing large displacements and forces with rapid response times have potential as haptic interfaces, especially those that can be implemented in thin form factors. Choices of designs that generate vertical (out-of-plane) vibrational displacements range from linearly contracting multilayer stacks to cantilevers, to pinned boundary configurations. This section highlights promising classes of EAPs, with a focus on materials, electrical characteristics and layouts optimized for vibratory actuation.

EAPs, as defined here, incorporate materials that operate through the action of Coulomb forces, induced polarizations

or motions of ions. Devices based on the first category typically use an electrical bias applied to a parallel plate capacitor formed with a low modulus polymer as the dielectric and deformable/stretchable conductors (e.g., carbon-impregnated grease) as the electrodes.^[119] The bias leads to electrostatic forces that compress the polymer to reduce the overall thickness of the structure and, by the Poisson effect, to increase its lateral dimensions. Important characteristics of electronic EAPs are their ability to operate stably in air with simple materials, to respond rapidly (within milliseconds), and to hold induced displacements under a DC voltage.^[120] The polymers in these devices are typically incompressible dielectric elastomers such as silicones and polyurethanes. The relatively low dielectric constants lead to high driving voltages (>1 kV) and corresponding electric fields (>100 MV m⁻¹), with operating limits set by electrical breakdown. Single-film dielectric elastomer actuators (DEAs) typically feature elastomer thicknesses in the range of 10–200 μm and offer maximum out-of-plane strains of 25–35%, corresponding to vertical displacements (contraction) of 3.5–70 μm .^[121–125] The lateral displacements correspond roughly to one half of these strains multiplied by the lateral dimensions of the actuators, typically in the range of 10–20 mm for representative devices used in haptics.

The linear elastic stretchability and the modulus of the elastomers, along with the structure of the actuator, are key properties that define the range of displacements that can be achieved and the maximum forces that can be applied. These two metrics represent important performance parameters, where displacement is the maximum distance of actuation when the actuator is operated without a load and the blocking force is the maximum force generated when motion of the actuator is completely blocked. Multilayer geometries can increase these parameters for a given driving voltage. The elastic restoring force of the polymer supports response times that can reach the ms range, relevant to vibratory operation for haptics, using appropriate voltage waveforms.

A representative vibrotactile DEA includes multilayers of silicone elastomer (8 layers, each 25 μm in thickness; CF19-2186, Nusil Company) separated with compliant carbon-film electrodes formed by spraying and drying a carbon powder solution through a mask, for a total thickness of 210 μm .^[126] Here, an array of 4 \times 5 actuators, each with a 2 mm in diameter, reside in a total area of 11 \times 14 mm². A hemispherical dome structure at each actuator forms a cavity with a height of 0.1 mm such that an applied electric field leads to a buckling deformation that alters the height of the cavity. Most DEAs for tactile stimulation purposes employ such structures.^[127,128] A voltage of 3.5 kV produces a displacement of 471 μm with a blocking force of 14 mN. An appealing feature is that these actuators are mechanically compliant and flexible, such that the entire array can be formed into a thimble shape as shown in Figure 3d. Viscoelastic effects reduce the displacements from ≈ 390 μm to ≈ 205 μm as the operating frequency increases from 0 to 100 Hz at a constant peak voltage of 2.5 kV. The maximum current level reaches ≈ 0.1 mA, corresponding to a peak instantaneous power consumption of 350 mW, but with a much lower time-averaged value for typical uses. Specifically, in dynamic applications like those in vibratory operation, power consumption increases linearly with the frequency, actuator capacitance, and square of applied electric field ($P_{\text{electrical}} = C_{\text{act}} V^2 f$, where C_{act} is the capacitance of the actuator when charged, V is the applied

potential, and f is the driving frequency). Based on this calculation, the electrical power input for a single DEA in the array described here is ≈ 25 mW for operation at 100 Hz.

A recent variant of the DEA is a device that exploits dielectric liquids sealed between a pair of flexible membranes with patterned conductive coatings. Application of a bias between these coatings causes the membranes to move together, in a zipping process that pushes liquid to create an out-of-plane displacement. Designs include conical-shaped cavities and deformable shells. The first type consists of a compliant electrode layer attached to a membrane of a dielectric elastomer that rests on top of a conductive chamber with a conical shape.^[129] The membrane zips down in the chamber upon application of a voltage between the electrode and the chamber body. The second type consists of a flexible polymer shell coated with flexible electrodes and filled with a liquid dielectric (i.e. silicone oil), referred to as hydraulically amplified self-healing electrostatic (HASEL) actuator.^[130–132] An applied voltage between the two facing electrodes causes zipping of the shell due to an electrostatic attraction, displacing the liquid dielectric against viscous resistance. A recent example of a vibrotactile actuator based on this type appears in Figure 3d. The device exploits membranes of polyethylene terephthalate and electrodes of Al (50 nm) on the periphery and on the bottom, referred to as hydraulically amplified taxel (HAXEL) actuator. A circular membrane of polydimethylsiloxane (PDMS) resides on the central-top region.^[133] A voltage applied between top and bottom electrodes zips the two, thereby pushing the liquid toward the central region to cause out-of-plane displacements that create a dome-shape. The actuator (6 mm in length, 6 mm in width, 2.5 mm circular diameter at the center) generates 300 mN force and displacements of 500 μm , with a response time of under 5 ms, at an operating voltage of 1.4 kV. The displacement decreases to 100 μm at 200 Hz, presumably due to effects of inertia and viscosity.

Other types of electronic EAPs include electrostrictive polymers, which respond with positive strains to electric fields due to the reorientation of randomly aligned chain backbones along the direction of the field.^[134,135] These interactions lead to strains that are proportional to the square of the electric field. Representative electrostrictive polymers include high-energy-electron irradiated (HEEI) poly(vinylidene fluoride-trifluoroethylene) (P(VDF-TrFE)) copolymers, electrostrictive graft elastomers (G-elastomer), and P(VDF-TrFE)-based terpolymers.^[136] An example of a commercially available film-type vibratory actuator (10 mm in length, 10 mm in width, 150 μm in thickness; Novasentis Inc.) uses an electrostrictive polymer in a multilayer geometry with 20–25 layers, each with a thickness of 3–5 μm and with electrodes on the top and bottom surfaces.^[137,138] A 50 μm thick layer of polyether ether ketone (PEEK) serves as an elastic substrate. The actuator mounts onto a flexible printed circuit board (FPCB) by attaching either one end of the film as a cantilever-condition or two facing ends as a pinned boundary-condition. Published examples include actuators mounted in the cantilever geometry with a free-end displacement of 526 μm for an input voltage of 150 V and a response time of 160 ms, with forces at frequencies that are within the range of human tactile perception (see Section 2). The power consumption peaks with a value of 378 mW and drops abruptly by an order of magnitude within 100 ms. As with DEAs, the time-averaged power consumption is comparatively low, ≈ 23 mW for 100 Hz operation.

Liquid crystal polymers represent another class of electronic EAPs, where the actuation follows from changes in the alignment of liquid-crystalline side chains. Such changes arise from application of an electric field or from a change in temperature, to produce dimensional changes of the polymer, and corresponding displacements of the actuator.^[116] The response times for field-driven actuation (≈ 10 ms) are considerably faster than those for thermally induced actuation (≈ 125 –500 ms for 100 μm thick film), where rates in the latter follow from considerations in thermal transport to the surroundings.^[115] Other drawbacks of liquid crystal polymers with thermally induced activation include low efficiency ($< 5\%$), ultimately limited by the Carnot efficiency, and requirements of continuous heating during activation periods. Field-driven liquid crystal polymers are promising due to high efficiency ($\approx 75\%$) and moderate field requirements (1.5–25 MV m^{-1}), but their maximum strains are relatively small ($\approx 4\%$).

Ionic EAPs, as an alternative to electronic EAPs, offer some potential as the basis for vibrotactile actuators.^[115,120,139] Actuation relies on swelling or contraction of a polymeric membrane based on motions of mobile ions under the influence of electric fields. Materials for such purposes include ionic polymer–metal composites (IPMC) and conducting polymers. A common IPMC actuator sandwiches a membrane of perfluorinated ionomers (e.g., Nafion and Flemion) with two metal layers (e.g., platinum and/or gold).^[140] After immersion of an IPMC actuator in water, application of an electric field attracts cations toward the cathode (i.e., positively charged ionomer).^[141] With anions anchored to the backbone of the polymer, this accumulation of positive charge generates an electrostatic strain and consequent bending of the entire structure. Conducting polymers for ionic EAPs feature conjugated structures (e.g., polypyrrole and polyaniline) that undergo dimensional change under the electrochemically changing oxidation states, due to the addition or removal of charges from the membrane and a balancing flux of ions.^[142] Typical devices based on ionic EAPs achieve displacements of 2–10 mm and forces of 0.5–50 mN at low operating voltages (1–10 V), but at high currents (hundreds of mA). The resulting high operating powers are a key disadvantage, as are requirements for aqueous operating environments to facilitate ionic transport. For these reasons, ionic EAP remain relatively underexplored for haptics.

3.2.3. Piezoelectric Polymer and Ceramic Actuators

Piezoelectrics are materials that undergo changes in polarization that produce electric fields in response to mechanical stresses or vice versa.^[143] The piezoelectric coefficient (d_{xy}), where “ x ” refers to the direction of the applied field and “ y ” is the axis of effective strain, with units of “meter per Volt” or “Coulomb per Newton,” is a tensor that captures the magnitude of this effect for different directions along the material and for different directions of the applied electric field or mechanical stress. In many actuators, the most important component of this tensor is denoted as “ d_{33} ,” corresponding to the strain that occurs in the polarization axis for an electric field in this same direction. Other coefficients include, as examples, d_{31} and d_{15} , which are measures of perpendicular and shear deformations to the polarization axis, respectively. In general, piezoelectric materials fall into three categories: crystals such as quartz,

ceramics such as lead zirconate titanate (PZT), and polymers such as polyvinylidene fluoride (PVDF).

PZT-based ceramics are in widespread use due to their ease of synthesis and their large piezoelectric constants.^[144–146] Doping PZT with donors and acceptors create different varieties of materials with properties that can be tailored to the application requirements. For example, PZT-5A is useful for applications at high temperatures but with reduced performance (374 pC N⁻¹ in d_{33}) compared to PZT-5H (593 pC N⁻¹ in d_{33}), which has the disadvantage of temperature dependent response. As comparison, the d_{33} of lead magnesium niobate–lead titanate (1– x)[Pb(Mg_{1/3}Nb_{2/3})O₃] $-x$ [PbTiO₃] (PMN-PT), a single-crystal alternative for high performance, is 2820 pC N⁻¹ (67% PMN and 33% PT).^[147,148] Barium titanate BaTiO₃ with a d_{33} of 191 pC N⁻¹ is a ceramic that is attractive for its lead-free composition.^[149]

PVDF is a polymeric alternative to these inorganic materials, of interest for its low modulus, high fracture strain, and ease of processability. The d_{33} is -271 pC N⁻¹, where the negative sign indicates that the thickness decreases upon application of an electric field in the direction of the poling field.^[150] This constant is positive for almost all piezoelectric materials except for PVDF and its copolymers with trifluoroethylene (P(VDF-TrFE)).^[151] PVDF exists in five crystalline polymorphs, the α -, β -, γ -, δ -, and ϵ -phases, that form in ways that depend on the processing details. The β -phase shows the strongest piezoelectric behavior, due to a significant dipole moment from an all-trans, planar zigzag conformation.^[152] Solvent casting methods, fiber electrospinning techniques, the addition of nucleating fillers, and the development of PVDF copolymers are among various techniques that can facilitate the formation of the β -phase.^[152] Films of β -phase PVDF can be obtained by transitioning the α -phase, which is obtained naturally in casting films, by stretching and poling under high temperature (80–150 °C).^[153–156] Polymer-inorganic composites, such as those that embed PZT fibers or BaTiO₃ nanocubes into a PVDF matrix, produce hybrid forms of films with a good balance between electrical and mechanical properties, suggesting potential applications in vibratory actuators.^[157–159]

A typical actuator consists of a thin film (50–1000 μ m in thickness) of a single or multilayer stack of piezoelectric material formed between pairs of electrodes in a parallel plate geometry, to produce a vertical displacement with a force upon application of a voltage, where the d_{33} piezoelectric constant defines the magnitude of the response. The electrical and mechanical properties, such as driving voltage, response time, displacement, and generative force depend on the material properties and structure, as well as the overall actuator design. The most widely explored materials for vibrotactile actuators are PVDF and PZT. The former is often favored due to its mechanically flexible and transparent properties and the latter to its high piezoelectric constant.

One example of a vibrotactile actuator array (8 \times 6) uses a β -phase, large-area film of PVDF (153 \times 93 mm²) with a thickness of 80 μ m and pairs of transparent electrodes of indium–tin–oxide (17 \times 14 mm²) on opposing sides of the film.^[160] An AC voltage with peak values between 500 and 1000 V leads to forces of ≈ 0.5 N and displacements that are detectable on the fingertips at 100 Hz (see Section 2).

As with DEAs, multilayer geometries can reduce the operating voltages and increase the displacements. In one case, an actuator using a stack of 25 layers of PVDF (each 20 μ m

in thickness) formed by doctor-blading an ink formulation in a ketone solvent, separated by silver electrodes, with dimensions of 35 \times 14 \times 2 mm³ and an active area of 12 \times 8 mm², operates at 200 V to provide a force feedback of 200 mN cm⁻² and a displacement of ≈ 2.5 μ m.^[161] Similar to DEAs, the power consumption of piezoelectric actuators increases linearly with frequency and capacitance. In this particular case, the power consumption is less than 3 mW for an AC input with an amplitude of 350 V and a frequency of 450 Hz.

Although the high piezoelectric coefficient of PZT is an advantage, its high modulus and low fracture strains represent key disadvantages relative to PVDF and related piezoelectric polymers for use as skin-integrated haptic devices. One strategy to overcome this deficiency exploits PZT layers with extremely small thicknesses and thin polymer encapsulation structures to achieve low bending stiffnesses necessary to conform to the surface of the skin.^[162,163] Figure 3e shows a scanning electron microscope (SEM) image of an array of such PZT sensors and actuators, integrated onto the surface of a replica of human skin. Fabrication begins with formation of a 500 nm thick film of PZT using sol-gel techniques and annealing at high temperatures on an oxidized silicon wafer. The sensors (100 \times 500 μ m²) and actuators (200 \times 1000 μ m²) include a bottom electrode (Ti/Pt, 20/300 nm), a PZT layer, and a top electrode (Cr/Au, 10/200 nm), defined by photolithography processes and wet etching techniques. Retrieval of the devices involves elimination of the underlying oxide layer with diluted hydrofluoric acid and application and removal of a thermal tape for release onto a separate layers of poly(methyl methacrylate) (PMMA; ≈ 50 nm in thickness) and polyimide (1.2 μ m in thickness). Coating another layer of polyimide (1.2 μ m in thickness) on top of the devices for protection, followed by formation of openings through the protection layer for access to metal electrodes and deposition of metal interconnects (Au/Cr, 200/10 nm) completes the structure. Eliminating the underlying PMMA layer with acetone and performing another transfer process with a thermal tape onto a 20 μ m thick film of silicone yields a device in a sufficiently thin format to allow direct coupling to the surface of skin. These structures provide an ability to apply forces to soft tissues and to monitor their resulting displacements as the basis for characterizing the mechanical properties. Because displacements are on the order of a fraction of a micron, thick, multilayer stacks of such devices are required to generate vibrational amplitudes sufficient for haptics.

Vibrotactile actuators based on PZT typically exploit one of three different multilayer configurations, often referred to as stack, bending, and cymbal actuators.^[164–166] The first incorporates multiple layers of PZT films assembled together in orientations that use deformations based on the longitudinal piezoelectric coefficient, d_{33} .^[167] Such multilayer techniques are similar to those used in DEA and electrostrictive actuators. One reported design offers a maximum force of 900 N, displacement of 10 μ m and a response time of 1–5 μ s for a driving voltage of 100 V in a system that incorporates 100 layers of thin PZT (100 μ m) sheets, with dimensions of 5 \times 5 \times 12.7 mm³.^[160] This configuration is nonideal for skin-integrated vibrotactile actuators due to the large required thicknesses and the resulting low bendability.

Bending actuators consist of cantilever beams with piezoelectric films in bimorph or unimorph configurations.^[168] Bimorph designs incorporate two piezoelectric plates with

polarization normal to the interface, such that one plate expands and the other contracts with applied electric field. Unimorphs use a single piezoelectric plate attached to a nonpiezoelectric elastic plate (i.e., passive plate) to induce a transverse deformation with applied electric field. The cantilever-style actuator (Novasentis Inc.) based on the electrostrictive poly(vinylidene fluoride–trifluoroethylene–chloroethylene) (P(VDF–TrFE–CFE)) terpolymer attached to a PEEK-based passive plate presented in Section 3.3.2 is an example of this unimorph configuration. For a piezoelectric bending actuator with dimensions of $12.7 \times 10 \times 0.6 \text{ mm}^3$ in a bimorph cantilever configuration with one end fixed, the tip can move with amplitudes of up to $35 \mu\text{m}$ and a maximum blocking force of $0.5\text{--}1 \text{ N}$ and response time of $100 \mu\text{s}$, under a driving voltage of 100 V .^[165] An example of a practical bending actuator (30 mm in length, 15 mm in width, 0.35 mm in thickness, 0.3 g in weight; PiezoHapt, TDK Electronics) uses a unimorph structure with electrodes that sandwich a $200 \mu\text{m}$ thick PZT layer ($20 \times 10 \text{ mm}^2$ in dimensions) on opposing sides.^[169] A $100 \mu\text{m}$ thick metal plate based on a Ni–Fe alloy with large lateral dimensions ($30 \times 15 \text{ mm}^2$) bonds to one side of the actuator, thereby enabling the entire plate to vibrate under an AC voltage of 12 V with a power consumption less than 5 mW , a response time less than 4 ms , and a displacement of $65 \mu\text{m}$. The blocking force is within the range of human tactile perception (see Section 2). A sine wave signal with a frequency of 200 Hz and a voltage of 12 V yields a maximum vibrational acceleration of 0.3 G (for a 100 g mass), which can be compared directly with ERM and LRA actuators (see Section 3.2.1).

A cymbal actuator consists of a single- or multilayer of circular piezoelectric disk sandwiched between two cymbal-shaped metal end caps.^[165] The cymbals, typically made with thin layers of brass or titanium and with lateral dimensions that match the disk, bond to the two opposing sides of the disk on the edges, such that cavities form between the cymbals and the disk. Application of an electric field triggers a lateral compression in the piezoelectric disk which converts into an axial displacement due to the flexural, bending motion of the cymbals in the vertical direction. Such designs provide characteristics intermediate between those provided by the stack and bending configurations.

One example of a vibrotactile actuator (9 mm in length, 9 mm in width, 1.1 mm in thickness, 0.3 g in weight; PowerHap, TDK Electronics) with this layout uses 23 layers of PZT (0.6 mm in total thickness), copper electrodes, and a titanium-based cymbal (8.7 mm in diameter, 0.1 mm in thickness) generates a displacement of $35 \mu\text{m}$ and blocking force of 3.0 N (60 V input), with a response time of less than 1 ms .^[170] A sine wave with a frequency of 200 Hz and a voltage of 60 V yields a maximum vibrational acceleration of 2.5 G (for a 100 g mass). The power consumption is less than 5 mW .

The resonant frequency for vibratory actuation depends on the stiffness, the thickness, and the mass of the piezoelectric material and the electrodes. Reducing the thickness, increasing the stiffness and reducing the mass all lead to increases in frequency. All classes of piezoelectric actuators require high drive voltages, although typically much less than those associated with DEAs. Driver ICs specifically developed for piezoelectric actuators are available for voltages of up to 200 V , using embedded amplifiers that have input voltages of $1\text{--}5 \text{ V}$.

3.2.4. Soft Pneumatic Actuators

Soft pneumatic actuators (SPA) operate by transferring air from a source to a deformable bladder.^[171–173] A typical device includes a thin membrane of an elastomer in a circular shape to seal an underlying reservoir. Modulating the pressure of air in the reservoir causes the membrane to inflate or deflate, much like a balloon. Such actuation techniques have structural advantages especially in tight spaces or on sensitive regions of the body where rigid and bulky components are nonideal. For example, pneumatic actuators composed entirely of soft materials in thin geometries, without hard materials or sharp edges typically found in electronic or conventional actuator components, can be used even at the most challenging locations on the skin such as between a residual limb and a prosthetic socket. Various electrical, mechanical, thermal, or electrochemical pumping mechanisms and active or passive valves control the flow into and out of these reservoirs to yield forces that can reach several Newtons or more.

In one example designed to incorporate into a prosthetic liner for arm amputees, air passed inside a silicone-based chamber with pressures in the range of tens of kPa generates 8.5 N of vibrotactile force across a circulate area with a diameter of 16 mm from an actuator with a thickness of 6 mm .^[174] A collection of regulators, sensors, and high-speed valves support vibratory actuations at frequencies up to 70 Hz . The air pressure, as well as the types of silicone materials that form the base of the SPA determine the pressure, displacement, and force of the actuation. SPAs with a given geometry but constructed with two different silicone formulations (type A: Dragon Skin 30, Smooth-On; type B: RTV-1520, Silika Moldes e Insumos) result in maximum pressures of 70 and 50 kPa , with displacements of 3.5 and 4.5 mm , and forces of 8.5 and 9.5 N for type A and type B, respectively.^[175] A dynamic analysis demonstrates that the response times and displacements at 10 Hz and 40 kPa of the type B device is faster (0.24 m s^{-1} vs 0.09 m s^{-1}) and larger (by 2 times) than the type A device. These differences follow from a higher (by 1.5 times) elastic modulus for the type B material compared to the type A.

A miniature soft pneumatic actuator of this sort, with dimensions comparable to actuators discussed previously, appears in Figure 3f.^[176] The main structural material in this case is PDMS, with an elastic modulus similar to that of human skin. The actuation region consists of an intermediate flexible mask layer (polypropylene; $50 \mu\text{m}$) sandwiched between two silicone layers, with a total thickness of $500 \mu\text{m}$. The lateral design of the intermediate layer adopts a spoon-like shape with a head diameter of 10 mm that forms the actuation region and a handle width of 2 mm that forms the channel for the air pump. This structure bonds to the bottom silicone layer to ensure that deformation occurs on the top PDMS layer, upon inflation through the channel. The top and bottom PDMS layers bond in the remaining regions. A pressure of 25 kPa generates a force of up to 1 N and an inflation height of 1.5 mm . A high-speed pressure regulator enables rapid inflation and deflation, for operation in a range of frequencies from 5 to 100 Hz . At 30 Hz , the vibration amplitude decreases to 70% of the maximum measured value, with further significant decreases as the frequency reaches 100 Hz . Whereas the physical geometry

and base material determine the static characteristics of SPA, such as the maximum pressure, displacement, and force, the high-pressure air source and regulator systems often limit the vibratory actuation, especially in a range of high frequencies. As with DEAs, viscoelasticity can dampen vibrational operation in this range.

3.3. Comparative Summary of Options in Haptic Stimulators

Table 1 summarizes examples of electro-tactile and vibrotactile actuators, organized according to their material properties, performance, and structure. Entries also include typical driving input parameters, as well as vibratory output

Table 1. Examples of electro-tactile and vibrotactile actuators organized according to their material properties, performance attributes, and design features.

Stimulation method	Type	Key materials and features	Dimensions [mm]	Mechanically compliant	Electrical input			Vibratory output ^{a)}
					Typical voltage [V]	Typical current [mA]	Overall power [mW]	
Electrotactile	Patch electrodes ^[91]	Conductive hydrogel contact with PVC/PES support	$L = 10\text{--}20$ $W = 20\text{--}30$ $T = 1$	Y	20–40 (pulse)	2	–	$J = \approx 0.5 \text{ mA cm}^{-2}$ (varies by subjects, skin region, and PWM)
	Epidermal electrodes ^[183,185]	Metal (Au) contact array with ultrathin silicone support	$D = \approx 2$ $T = 0.03\text{--}0.06$	Y	30–50 (pulse)	1–3	–	$J = 5\text{--}30 \text{ mA cm}^{-2}$ (varies by subjects, skin region, and PWM)
Electromagnetic	Coin-cell ERM ^[100]	Internally rotating W alloy mass with Cu coil and NdFeB magnet	$D = 6\text{--}12$ $T = 1.8\text{--}3.4$	N	2.5–3 (DC)	27–78	–	$a_v = 0.25\text{--}3.0 \text{ G}$ (depends on size) d_0 and F_B not available
	Coin-cell LRA ^[108]	Moving NdFeB magnet with Cu coil and steel wave spring	$D = 6\text{--}12$ $T = 1.8\text{--}3.7$	N	1.2–2.0 (AC)	28–69	–	$a_v = 0.7\text{--}1.9 \text{ G}$ (depends on size) d_0 and F_B not available
	Flexible voice-coil actuator ^[51,187]	Cu/Au coil and moving NdFeB magnet framed with PDMS body	$D = 15\text{--}18$ $T = 2.5\text{--}4.0$	Y	5 (pulse)	5–150	–	$d_0 = \approx 191\text{--}300 \mu\text{m}$ F_B and a_v not available
Dielectric elastomer	Small dome-shaped actuator array ^[126]	8 layers of silicone separated with stretchable carbon-film	$D = 2$ $T = 0.2$	Y	3500 (AC)	–	25	$d_0 = \approx 471 \mu\text{m}$ $F_B = 14 \text{ mN}$ a_v not available
	Large dome-shaped actuator array ^[128]	6 layers of PDMS separated with stretchable AgNW film	$D = 16$ $T = 0.7$	Y	3000–4000 (AC)	–	–	$d_0 = \approx 300\text{--}650 \mu\text{m}$ $F_B = 50\text{--}250 \text{ mN}$ a_v not available
Piezoelectric	Unimorph electrostrictive polymer actuator ^[138]	25 layers of P(VDF-TrFE) mounted on polyether ether ketone (passive)	$L = 10$ $W = 10$ $T = 0.15$	Y	150	–	23	$d_0 = 526 \mu\text{m}$ F_B and a_v not available
	Single layer polymer actuator ^[160]	PVDF sandwiched with transparent ITO electrodes	$L = 17$ $W = 14$ $T = 0.08$	Y	500–1000 (AC)	–	–	$F_B = 500 \text{ mN}$ d_0 and a_v not available
	Multilayer polymer actuator ^[161]	25 layers of PVDF separated with Ag electrodes	$L = 12$ $W = 8$ $T = 2$	N	200–350 (AC)	–	3	$d_0 = 2.5 \mu\text{m}$ $F_B = \approx 190 \text{ mN}$ a_v not available
	Unimorph ceramic actuator ^[169]	PZT mounted on Ni-Fe alloy plate (passive)	$L = 30$ $W = 15$ $T = 0.35$	Y	12 (AC)	–	5	$d_0 = 65 \mu\text{m}$ $a_v = 0.3 \text{ G}$ F_B not available
	Cymbal ceramic actuator ^[170]	23 layers of PZT separated with Cu electrodes and mounted with Ti cymbals	$D = 8.7$ $T = 0.1$	N	60 (AC)	–	5	$d_0 = 35 \mu\text{m}$ $F_B = 3.0 \text{ N}$ $a_v = 2.5 \text{ G}$
Soft pneumatic	Large SPA for prosthetic liner ^[174]	Air chamber created with two silicone membranes and fabric	$D = 16$ $T = 6$	Y	–	–	–	$F_B = 8.5 \text{ N}$ d_0 and a_v not available
	Miniature SPA ^[176]	Spoon-like air chamber created with two PDMS membranes and flexible polypropylene	$D = 10$ $T = 0.5$	Y	–	–	–	$d_0 = 1.5 \text{ mm}$ $F_B = 1.0 \text{ N}$ a_v not available

^{a)}J: current density; d_0 : no-load displacement; F_B : Blocking force; a_v : vibrational acceleration for a 100 g mass.

parameters, such as current density for electrotactile stimulators, and displacement, maximum blocking force, and peak vibration amplitude for vibrotactile actuators. ERMs and LRAs are commercially available, including some with drive ICs in integrated packages with waveform generators and amplifiers, and therefore currently represent the simplest, most reliable, and most accessible components for exploring various system level considerations. Potential improvements for skin-integrated formats include replacing the rigid, heavy metalized housings of these actuators, along with the associated drive electronics, with soft, skin-compatible alternatives to minimize the mechanical mismatch between the devices and the body. A challenge is in interfacing materials that also efficiently transmit vibrations, without significant damping. Voice coil- and inorganic piezoelectric-based vibratory actuators also exist, but with comparatively low levels of maturity and availability. Soft encapsulation techniques are common for voice coil-based actuators in skin-integrated haptics, but requirements for conventional magnets prevent realization of entirely soft, compliant devices. Similarly, the multilayers used in traditional inorganic piezoelectric actuators typically also lead to rigid overall structures. EAPs and polymer piezoelectrics are attractive due to their flexible mechanics, large actuation strains, fast responses, and high energy densities, but particularly in the case of EAPs, the high voltage requirements create safety concerns and practical difficulties in the design of drive electronics. Pneumatic actuators have various attractive features, but they are also in their infancy as haptic interfaces and their scalability is limited by requirements for pumping and valving technologies, many of which are poorly suited for skin-integrated or wearable applications due to their weight and bulk. Given serious drawbacks associated with nearly all existing options, many opportunities exist for research on unusual materials and device structures for skin-integrated vibrotactile actuators. In addition, the criteria for practical skin-integrated electronics are demanding, as safety and tactile sensation thresholds must be considered carefully. The following sections review vibrohaptic interface systems that utilize some of the most promising actuation methods discussed here.

4. Progress in Skin-Integrated Vibrohaptic Interfaces

Important performance characteristics of vibrohaptic interfaces that adopt the arrayed, skin-integrated characteristics envisioned here include low power consumption, wireless control, fast spatiotemporal response, lightweight construction, thin layouts, and soft, flexible mechanics. In this context, battery-free operation can be an important, although not essential, additional feature. The systems must not induce irritation at the skin surface and must offer high levels of safety from the standpoint of electrical leakage, radio-frequency exposure, and thermal load, while at the same time and ability to generate strong forces, large amplitudes and broad ranges of vibratory frequencies. This set of demanding requirements can only be addressed through advanced materials and innovative engineering approaches.

4.1. Skin-Integrated Vibrohaptic Interface Based on Electrotactile Stimulators

Many types of haptic interfaces use electrotactile mechanisms, ranging from touch screen displays that also support programmable tactile sensations, to controllers for human-computer interactions, to robotic prosthetics with sensory feedback.^[90,177,178] Although electrotactile mechanisms offer simplicity in design and operation, their use in imitating real-world tactile cues demand active control over the stimulation intensity across narrow ranges, with built-in safety measures to prevent excessive stimulation that can result from natural fluctuations in the electrode-skin impedance, as suggested previously. Mild, or even insensible, levels of sweating or changes in the hydration state of the skin can change its intrinsic electrical characteristics and, therefore, the impedance.^[91] The electrodes themselves can undergo mechanical/electrical fatigue or their adhesion to the skin can degrade due to natural motions or processes (e.g., exfoliation of dead cells from the stratum corneum), also with associated effects on the impedance. The designs and construction aspects of the electrodes, the choices of materials and the safety control systems are, thus, essential in achieving both mechanically and electronically stable electrotactile stimulators, especially in applications, like those in VR/AR, that require fast and precise control over sensations. **Figure 4** presents some examples of skin-integrated electrotactile interface methods, including those that use techniques to adjust impedance levels through advanced controllers, fabrication strategies to improve skin-conformality, and material choices to allow stimulation with high spatial densities. The following sections describe associated considerations and recent work to address some of these issues.

4.1.1. Controlling Sensation Intensity of Electrotactile Stimulation

In addition to the effects mentioned above, where the intensity of an electrotactile sensation can change over time due to biological or electronic effects, the nature and strength of the perception depends strongly on variations across individuals. Psychophysical experiments based on electrotactile stimulations on the stump skin of the forearms of amputees, and in separate studies on the arms of able-bodied subjects, highlight mean perceptual thresholds for six distinct sensory modalities: touch, pressure, buzz, vibration, numb, and pain.^[178] Sensations of touch and pain correspond to minimal detectable sensation and maximal endurable pain, respectively. Stimulation involves two electrodes (25 mm in diameter) as active and reference, with nominal current amplitudes of 3.75 mA, pulse widths of 200 μ s (200 μ s interpulse delay) and frequencies of 50 Hz. The active electrodes are on the stump skin of the forearms for amputees and on the frontsides of the upper arms for able-bodied participants. The reference electrode is at 10 cm above the elbow crease of the same stump for amputees and on the backside of the upper arm for able-bodied participants. The mean thresholds of amputees, in terms of current densities, are 0.21 mA cm⁻² for touch, 0.28 mA cm⁻² for pressure, 0.39 mA cm⁻² for buzz, 0.49 mA cm⁻² for vibration, 0.66 mA cm⁻² for numb, and 0.90 mA cm⁻² for pain.

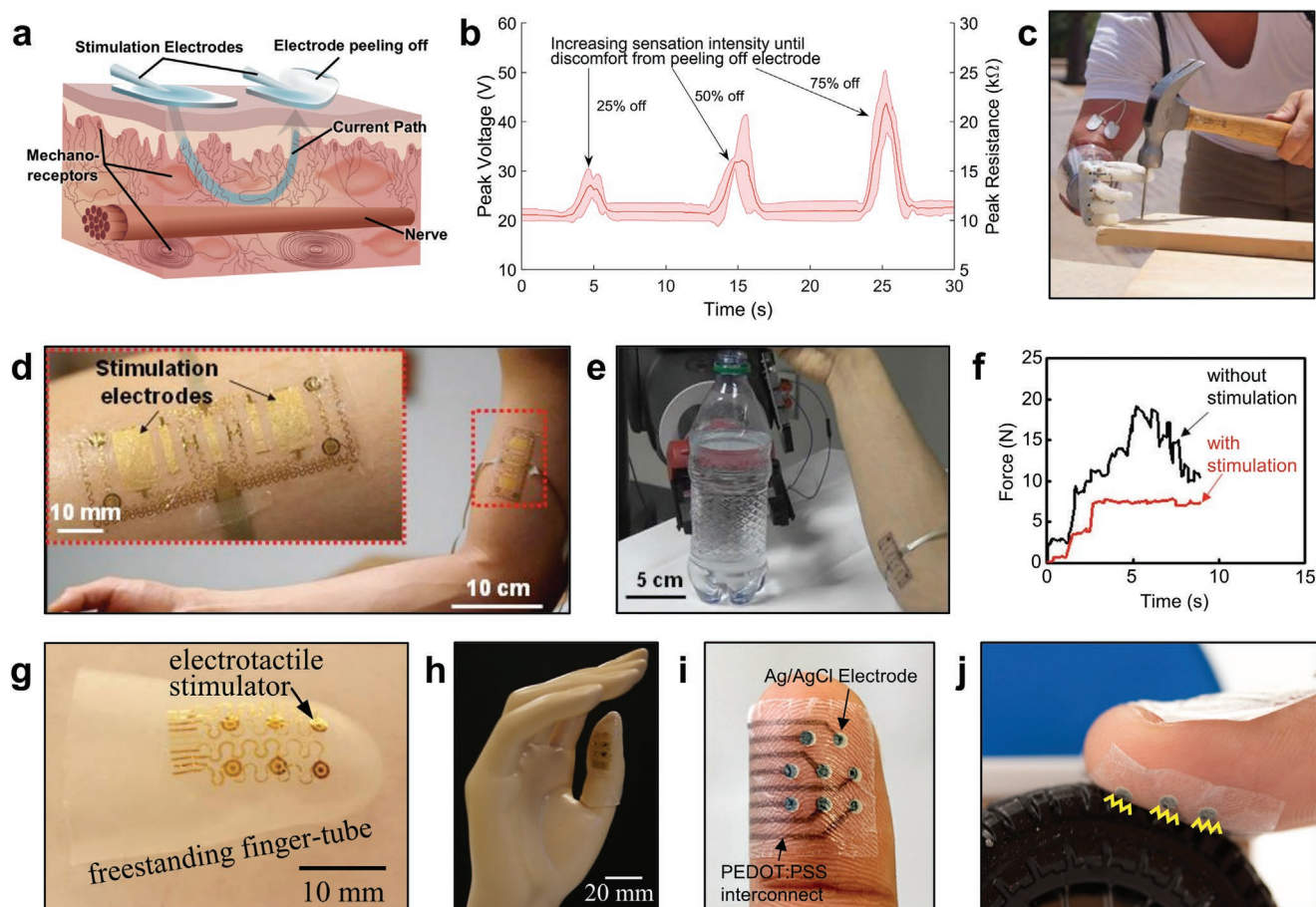


Figure 4. Skin-integrated electro-tactile stimulators. a) Schematic illustration of the process of electro-tactile stimulation with two electrodes. Currents that flow across the afferent nerves in the skin produce sensations. As the electrode gradually peels away from the skin, the current density for a constant applied voltage increases, resulting in an enhanced sensation. b) Changes in the peak resistance of the electrode–skin interface due to peeling and reapplying the electrode. As the electrode peels from the skin, the sensation increases and ultimately leads to discomfort. The results show the mean and SD of experiments over five trials. c) Photograph of a participant with below-elbow amputation using a prosthesis with electro-tactile touch feedback during a hammering of a nail. Reproduced with permission.^[91] Copyright 2018, The American Association for the Advancement of Science. d) Photograph of large-area electrodes mounted on the biceps for muscle stimulation. The inset shows a magnified view. e) Photograph of an electro-tactile stimulator on the forearm during operation while the participant controls a robot arm to grip a bottle filled with water. f) Gripping forces with (red) and without (black) stimulation feedback. With electro-tactile feedback, the participant can grip the bottle in a controlled manner, to prevent collapse. Reproduced with permission.^[183] Copyright 2015, Wiley-VCH. g) Photograph of a multiplexed array of electro-tactile stimulators on the outside of an elastomeric finger-tube. Turning the tube inside out relocates the array on the inner surface of the finger-tube to allow contact with the skin. h) Photograph of a multifunctional, skin-integrated system for electro-tactile stimulation with electrode arrays multiplexed using silicon nanomembrane (Si NM) diodes, high-sensitivity strain monitoring with Si NM gauges, and tactile sensing with elastomeric capacitors on the anterior of the thumb. Reproduced with permission.^[184] Copyright 2012, Institute of Physics. i) Photograph of a skin-worn electro-tactile device with Ag/AgCl electrodes conformally mounted on a fingertip. j) Photograph of a fingertip with an electro-tactile device touching a physical model of a car. Reproduced under the terms of the Creative Commons CC BY 4.0 License.^[185] Copyright 2018, the Authors. Published by Association for Computing Machinery.

Depending on the individual, the lowest and highest threshold for touch is 0.16 and 0.33 mA cm⁻², and for pain is 0.73 and 0.99 mA cm⁻², respectively. The mean thresholds for the able-bodied subjects are similar for touch, but significantly lower for pain (0.72 mA cm⁻²).

Research also suggests that there is a strong dependence of the tactile thresholds on the distance between electrodes and on body location, given differences in skin impedance and densities of afferent nerves.^[7] Specifically, the ratio of current threshold for “pain” to “touch” varies from 1.5 to 1.6 for the fingertip to 5–10 for the abdomen. Difficulties in determining thresholds arise from the absence of a uniform definition

for pain and from variations in methodologies between the experiments. One study suggests that large electrodes induce greater stimulation-related discomfort than smaller electrodes at equivalent current densities. Specifically, at a current density of 0.043 mA cm⁻², the perceived intensity of large electrodes (35 cm²) exceeds by nearly two times that of small electrodes (16 cm²).^[180] These results suggest that practical use might require individually optimized settings, determined empirically from tests and subject reports for a given pair of electrodes, body locations and stimulation waveforms.

Figure 4a illustrates one of the simplest effects, where a decrease in contact area of a partially delaminating electrode

leads to an increase in impedance, and therefore an associated increase in the spatial concentration of current injected through the skin in the contacting regions, for a given applied voltage.^[91] In the absence of fast control electronics, such delamination effects, particularly if they occur suddenly, can lead to current spikes and associated pain or electrical shock. Typical electro-tactile stimulation involves current pulses with durations that are too short to reach a steady state or to adapt/modify in real time. The peak resistance is defined by dividing a peak voltage (V_p), in response to a current pulse, by the current amplitude. As a specific example, at a V_p of 20 V, estimated using a current stimulation waveform with 2 mA current (I), 200 μ s pulse duration (T) at 20 Hz, through two electrodes each with dimensions of 28×20 mm², over 5 trials, the mean peak resistance (R_p) is ≈ 11 k Ω . A delamination of 25%, 50%, and 75% of the area of the stimulation electrode increases the mean R_p to ≈ 14 , 16, and 22 k Ω , with corresponding changes in the mean V_p to ≈ 27 , 32, and 44 V (Figure 4b), respectively. The current densities would then likely vary in a corresponding manner, moving from thresholds for 0.36 to 1.43 mA cm⁻² across this range. The relationships for phase charge (Q) and peak pulse energy (E_p) with stimulation parameters of a monophasic square wave are $Q = IT$, and $E_p = R_p I^2 T$, respectively.^[181,182]

To compensate, advanced controller electronics implemented in the device can regulate the perceived sensation intensity regardless of the impedance change at the interface by modulating the stimulation parameters (I and T) immediately upon an impedance change.^[91] For example, lowering the current amplitude in response to a delamination event to maintain constant current density minimizes the variability in perceived sensation. Designing a controller that automatically adjusts these parameters requires precise understanding of the relationship between the stimulation parameter, impedance, and perceived sensation. Studies that quantify these effects rely on groups of participants, each of whom adjusts stimulation parameters in response to changes in perceived sensation intensity. One example involves ten participants with two pairs of electrodes, each pair consisting of active and reference electrodes, placed in the same location but on contralateral sides of the body. With initial stimulation parameters matched on both pairs, increasing T (e.g., from 200 to 700 μ s with 50 μ s increment; 50 Hz in frequency) on one pair (i.e., test pair) increases V_p , thereby changing R_p and the sensation intensity. Subsequently, the participants select and adjust amplitudes of current pulses, I , of the test pair to match reference sensation intensities on the other pair, under eight experimental conditions, with changes in session days, magnitudes of sensation, stimulation locations, pulse duration, and electrode sizes. Collecting the values of I and V_p , corresponding to each value of T , with the same perceived magnitude of sensation reveals linear relationships between E_p and R_p and between Q and R_p . Fitted lines constrained to the measured points show strong correlation coefficients (>0.9) for both relationships. The result is a set of linear plots (E_p vs R_p and Q vs R_p) across each participant that represents constant sensation intensity.

These results form the foundations for a model that uses computed slopes of the constant intensities to enable application of modulated current amplitudes and pulse durations to

compensate for any changes in impedance, thereby actively regulating the sensation intensity to minimize variabilities. For example, if R_p changes due to a mechanical disturbance, such as a peel-off, the E_p and Q deviate from the linear relationship, corresponding to a change in sensation intensity. A controller implemented with the model immediately regulates stimulation parameters to prevent such deviations. Various tests, including those that use electroconductive gels and sweating to alter the impedance, highlight the effectiveness of this approach. This type of controller functions well during daily activities, including ascending and descending flights of stairs, hammering nails into wood (Figure 4c), and exercising on an elliptical trainer, as mixed conditions of mechanical disturbances and sweating at the electrode–skin interface. Limitations are in regulating changes in sensation intensities under large changes in impedance (>40 k Ω) and in effects caused by nerve adaptation or psychophysical effects that are not reflected with impedance. The utility is also restricted to certain individuals and electrode sizes and placement locations. Further refinements in the electronics and/or in the development of materials that provide stable impedances even with changes in the properties of the skin may be needed. Considerations and possibilities for this latter strategy appear in the next section.

4.1.2. Materials and Designs for Skin-Integrated Electrotactile Electrodes

Most skin-integrated electrotactile electrodes are vulnerable to delamination due to the mechanical and geometrical mismatch between the materials for the electrodes and the skin, and to interfacial forces that arise from natural motions, like bending, stretching, and twisting, further increased by forces that pass through wired connections to external electronics. Commercially available electrodes (see Section 3.1) typically use gel- or woven-type patches with centimeter-scale areas and millimeter-scale thicknesses. An attractive form of skin-integrated electrotactile stimulator system adopts the physical properties of the skin itself for improved ability to conform to the relief on the surface of skin and the curved textures of the body, sometimes referred to as epidermal electronics. One popular such approach integrates patterned metal traces with stretchable serpentine-shaped filamentary geometries and microelectrodes with supporting electronics on thin elastomeric substrates.

An example of this type of epidermal stimulation electrode consists of a 200 nm thick concentric metal layer that has an inner disk (1.0 mm in radius) and an outer ring (2.0 mm in radius), with a 0.5 mm space in between.^[183] Fabrication begins with the formation of a sacrificial layer (PMMA; ≈ 100 nm in thickness) on a silicon wafer as a support for a layer of polyimide (1.2 μ m in thickness). Sputter deposition of metal (Cr/Au, 5/200 nm), followed by photolithography and wet etching processes define the outer ring (i.e., anode) of the stimulator. Another coating of polyimide (1.2 μ m in thickness), sputter deposition of metal (Cr/Au, 7/300 nm), and photolithography and wet etching forms the inner disk (i.e., cathode). A final encapsulation layer (polyimide; 1.2 μ m in thickness) patterned and etched with contact holes at the locations of regions that form the skin interface completes the device structure.

Dissolving the PMMA using acetone enables retrieval of the entire structure onto a water-soluble tape for transfer-printing onto a low modulus silicone elastomer sheet ($\approx 30 \mu\text{m}$ in thickness, $\approx 60 \text{ kPa}$ in modulus, $\approx 900\%$ in fracture strain; Ecoflex).

Compared with a widely utilized commercial stimulation electrode (Ambu Neuroline 700) that uses a soft hydrogel layer ($\approx 200\text{--}300 \text{ kPa}$ in modulus, $\approx 1 \text{ mm}$ in thickness), this epidermal system has a considerably lower modulus and reduced thickness; these two factors lead to a bending stiffness that is a factor of more than three million times lower. These characteristics are similar to those of the skin itself, to allow a robust, nonirritating, and conforming interface that is compatible with natural body movements and interfaces across nearly any region of the skin. Figure 4d shows an image of such stimulation electrodes attached onto the biceps. The maximum strain induced in the materials for the serpentine-based interconnects and electrodes, under a stretching deformation of 21%, is below 0.3%, which is within the elastic regime of gold.

Figure 4e shows a subject controlling a robotic arm using stimulation signals obtained from EMG as a sensory input to control the force of gripping a water bottle. The EMG sensor, fabricated using same procedures of the electro-tactile stimulator, lies alongside the stimulation electrodes, thereby combining both features in a single, epidermal electronic platform. A force sensor attached to the gripper of the robotic arm measures the applied force between the water bottle and the gripper, and this information passes to the subject in the form of an electro-tactile feedback. The stimulation delivers sensory input at a level proportional to the force measured by the sensor. Without this type of feedback, the subject is unable to effectively control the gripping force of the robot, causing the water bottle to collapse during the gripping process. By contrast, with feedback the subject can gently and moderately grip the water bottle in a well-controlled manner. A plot in Figure 4f shows the measured forces of gripping the water bottle with and without electro-tactile feedback, demonstrating random peaks and relatively higher applied forces in the latter case that lead to collapse. Here, the maximum current applied to the electrodes of 2 mA, corresponds to a maximum gripping force of 27 N.

This multifunctional platform also enables the control of virtual arms presented on a computer screen and physical robotic arms using proprioceptive feedback. Mounting two devices, one over the long head of the biceps brachii and the other on the lateral head of the triceps brachii muscles, allows control of the arms through an angular range between -60° and 60° based on EMG signals obtained from flexing or extending the elbow joint. Adding electro-tactile feedback significantly improves the performance, by decreasing mean absolute errors, computed using two-way analysis of variance (ANOVA), from 31.6° without feedback to 16.9° with feedback. Conventional technology approaches also provide similar improvements but only with multiple sets of separate, standard electrodes and wired connections.

Use of a layer that presses the electrodes against the skin can further improve the contact of electro-tactile electrodes beyond that possible with van der Waals interactions or adhesives. A silicon-based multiplexed array of electro-tactile stimulators placed in the interior surface of an elastomeric sheet in closed-tube fingertip geometry represents an example of this type of strategy, to

support high spatiotemporal resolution and improved mechanical stability (Figure 4g).^[184] Similar to the system introduced in Figure 4d–f, ultrathin electrodes ($\approx 500 \mu\text{m}$ in total thickness) and serpentine metal traces for stretchable interconnects form a skin-integrated fingertip electro-tactile device. Specifically, the electrodes use a concentric design with an inner disk ($400 \mu\text{m}$ in radius) and an outer ring ($1000 \mu\text{m}$ in radius), with a $250 \mu\text{m}$ space in between and thickness of 600 nm . The fabrication follows procedures similar to those of the epidermal electro-tactile stimulator described in Section 4.1.2, but with the addition of silicon nanomembrane (Si NM) diodes ($225 \times 100 \mu\text{m}^2$ in lateral dimensions and 300 nm in thickness) to facilitate matrix type readout and addressing. Fabrication uses silicon-on-insulator wafers and standard silicon processes to yield devices that have PIN (p-doped/intrinsic/n-doped) configurations. Eliminating the oxide layer allows transfer printing of these diodes to a layer of polyimide. An interconnect layer ($100 \mu\text{m}$ in width, 600 nm in thickness) then connects the diodes with concentric electrodes for a multiplexed array. Each diode supports stable electro-stimulation with input voltage up to 20 V and 0.25 mA current.

Placing the device inside of an elastomeric tube ($500 \mu\text{m}$) that is specially designed to match the geometry of the fingertip creates an intimate contact between the skin and electrodes, and secures the stimulators on the skin. A soft silicone elastomer (Ecoflex) (see Section 4.1.2) serves as the base material of the finger tube, in a form defined by pouring a polymer precursor onto a finger model and curing at room temperature for 1 h (repeated 3 \times ; $\approx 125 \mu\text{m}$ in thickness each). An important step in the fabrication involves flipping the tube inside out, such that devices initially attached on the outer surface move to the inner surface. This reversal induces a maximum strain of $\approx 30\text{--}40\%$ on the inner and outer surfaces, thereby requiring careful, computationally guided designs that minimize strains in the materials, of particular importance in avoiding damage to brittle materials such as silicon (fracture strain of $\approx 1\%$). Orienting the short dimensions of the diodes parallel to the flipping direction minimizes these strains. A mesh structure of serpentine interconnects is also important. These design optimizations lead to maximum strains of only 0.051%, 0.10%, and 0.040% for the gold, polyimide, and the silicon, respectively. In addition to the electro-tactile features, strain, and tactile sensors mounted on the outer surfaces of the elastomeric tube suggest options for incorporating additional electronics into the system for multifunctional operation (Figure 4h).

Another type of electro-tactile device for the fingertip features a “feel-through” interface that allows sensations from natural tactile stimuli to pass directly through the device, by using concepts in epidermal device construction and ultrathin temporary tattoo paper ($\approx 4.5 \mu\text{m}$ in thickness; Silhouette Temporary Tattoo Paper) as the substrate (Figure 4i).^[185,186] The electro-tactile stimulator ($10 \times 10 \text{ mm}^2$) contains an array of 8 circular electrodes with a 4 mm center-to-center spacing. The fabrication begins with screen-printing of a pattern of PEDOT:PSS electrical traces with $2 \mu\text{m}$ thickness and $500 \mu\text{m}$ width on the tattoo paper for electrical connections of the electrodes to contact pads for external control and power supply. Another screen-printing process forms an array of 8 circular electrodes based on a Ag/AgCl ink, each with a 2 mm in diameter and $20 \mu\text{m}$ in thickness. A layer of polyurethane- and epoxy-based insulator together with a skin

adhesive yields a total thickness of $\approx 10\ \mu\text{m}$ to encapsulate the device everywhere except at the regions of the electrodes. In an integrated layout, the total thickness is $\approx 35\ \mu\text{m}$ in the region of the Ag/AgCl electrodes and $\approx 15\ \mu\text{m}$ in the other areas. As the adhesive layer bonds with the skin, the height difference between two regions slightly stretches the area of the electrode-surrounding ring to create a microspring mechanism that pushes the electrodes onto the skin for consistent electrical contact.

The soft materials and ultrathin design allow the users to feel real objects and surfaces through the device without significant mechanical obstruction. In combination, a tactile sensation generated by the electrotactile stimulator allows the user to feel both the touched object as well as the artificial sensation. Figure 4j shows an example of this feature, where the subject wearing the ink-based electrotactile device perceives natural textures, shapes, and interactive elements of a tire through the device, as well as imitated vibrations of the car engine generated from electrotactile feedback.^[185] A key limitation is a lifetime limited to $\approx 8\ \text{h}$ in an office environment due to effects from water, such as sweat, that degrade the PEDOT:PSS and skin-tattoo paper interface.

4.2. Skin-Integrated Vibrotactile Interface Based on Electromagnetic Actuators

As mentioned in previous sections, mechanical actuators can directly activate mechanoreceptors in the skin to produce sensations without risks of electrical shocks or pain associated with electrotactile stimulation techniques, in a way that also bypasses many of the associated sources of variability. Electromagnetic motors or voice coils deliver sinusoidal oscillation of mechanical pressure to initiate tactile sensations, in packages that can be simple and highly reliable. Vibration intensities can be controlled through current magnitudes, pulsation characteristics, or oscillation frequencies. The devices are available in small form factors (i.e., ERM and LRA), such as millimeter-scale mini-actuators (see Section 3.2), or in customized voice coil-based forms that eliminate rigid components like metal casings, as described next.

4.2.1. Materials and Designs for Flexible Electromagnetic Actuators

The structure and components of an electromagnetically driven voice coil-based actuator that incorporates a mechanically compliant structure follow the basic principles described in Section 3.2.1.^[187] The device is similar to a conventional LRA, but replaces metalized parts like voice coil, casing, and spring, with FPCB, elastomeric body, and polymeric film, respectively, to yield a flexible form of actuator more well suited for skin-integration. The fabrication process begins with electroplating gold to a thickness of $16\ \mu\text{m}$ on photolithographically defined spiral patterns of metal (Cr/Au, 20/50 nm) to form a coil with 45 turns supported by a $50\ \mu\text{m}$ thick FPCB of polyimide. A separator of polyvinyl chloride (PVC) mounts on this FPCB using a transparent adhesive (Loctite). A cantilever also formed using PVC holds a 2 mm thick neodymium magnet at the center, mounted on a ring-shaped body of PDMS with

an inner diameter, outer diameter, and height of 15, 20, and 3 mm, respectively. This structure attaches on top of the voice coil with the separator in between. A skin-contacting layer of polylactic acid in a dome-like shape and a diameter of 1 mm mounts on top of the exposed region of the cantilever to expose vibratory movement of the magnet toward the skin. The overall structure secures the freely moving magnet at the center of the coil to maintain a straight vertical motion within the concentrated magnetic fields.

The finalized actuator has an operating frequency range of 10–200 Hz and a current range of 30–150 mA, with a maximum displacement of $\approx 191\ \mu\text{m}$ and a resonant frequency at 40 Hz. The displacement decreases significantly as the frequency is increased. An average displacement at 150 Hz and 150 mA is $5\ \mu\text{m}$, for example. The actuator generally achieves higher displacements ($>50\ \mu\text{m}$) at lower frequencies ($<90\ \text{Hz}$). A psychophysical experiment based on 20 participants reveals that the device generates the strongest and most convenient vibration at around 60 and 70 Hz. A ring-shaped piezoresistive sensor that has inner and outer diameter of 3 and 10 mm, respectively, comprised of a polymeric piezoresistive film impregnated with carbon black ($100\ \mu\text{m}$ in thickness; Velostat) sandwiched with FPCBs, attaches on top of the actuator. The integrated sensor and actuator enable touch sensing and vibrotactile feedback at the same location. The following section describes the use of this type of device in a skin-integrated platform.

4.2.2. Design Strategies for Skin-Integrated Electromagnetic Actuators

A combination of tactile sensing and feedback creates unique opportunities for future applications of VR/AR.^[187] The actuator/sensor individually attaches onto the fingertips of a lightweight, 3D-printed polyurethane-based flexible film (4 MPa in strength; Ninjabflex) printed to match the shape of a hand. A finger cap made using neoprene fabric overlays each fingertip, to secure the actuator on the palmar side of the fingertips as the user slides the fingers inside, by firmly contacting actuator/sensor against the skin.

With each actuator/sensor mounted on the index, middle, and ring fingers, this system forms a communication tool based on modified Braille alphabetic writing platform. Assigning each fingertip to a dot of the Braille (6 dots in total) gives the users the ability to create six dots combinations using both hands for representing English alphabets. A series of Braille codes to describe a word or a sentence can be sent by tapping on a hard surface, captured using the sensors, and delivering impulses wirelessly to the receiver's glove to reproduce corresponding vibration patterns via the fingertip actuators. Here, Bluetooth systems attached on the wrists support wireless communication. Data from a pool of subjects including 10 deaf blind and 10 nondisabled subjects indicates an accuracy of $\approx 70\%$ in communicating a few words. Although this system is currently restricted to the fingertips and relatively narrow application possibilities, scaled platforms of this general type might have relevance for immersive VR/AR experiences in the future.

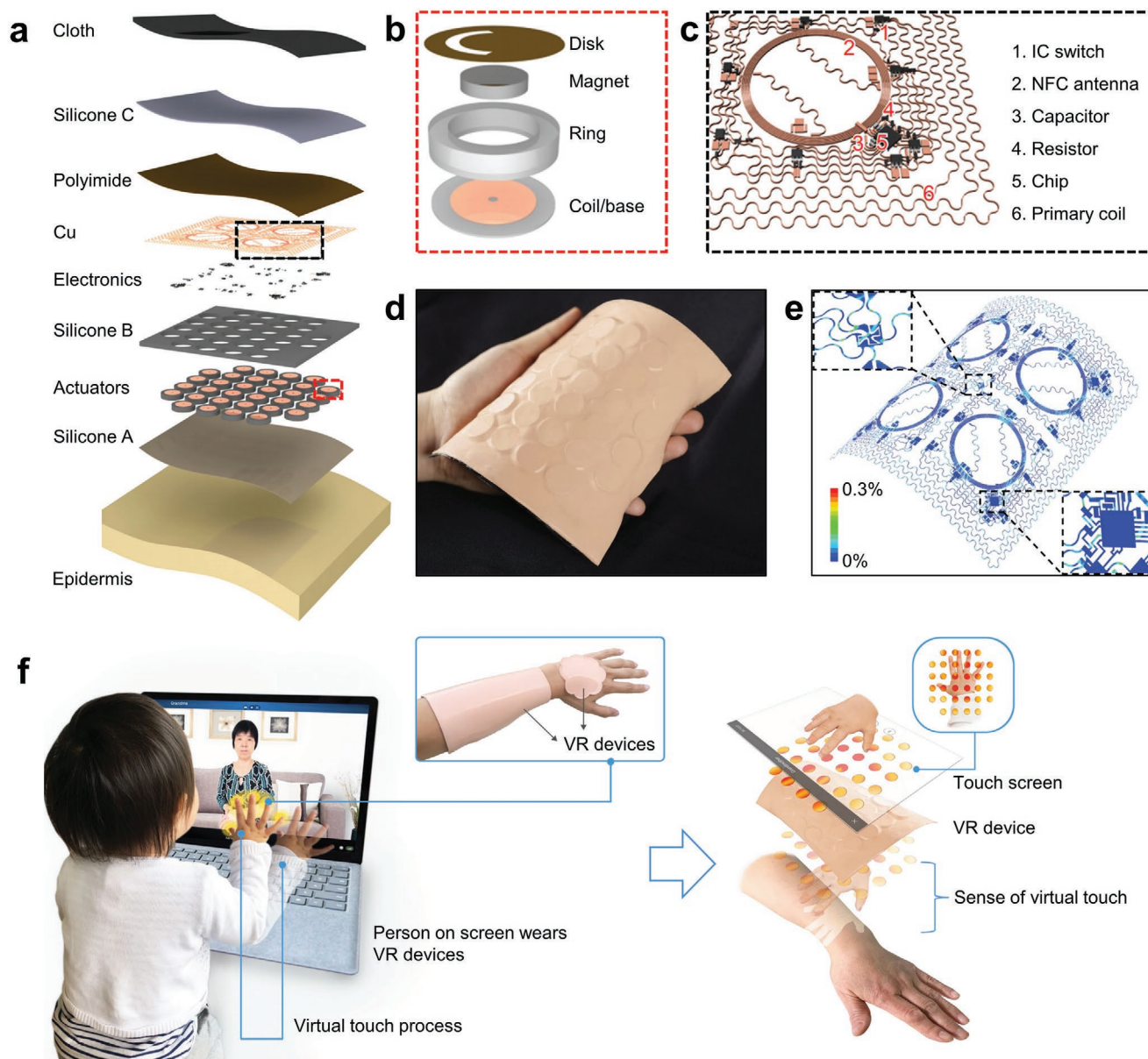


Figure 5. Skin-integrated electromagnetic vibratory actuators based on voice-coils. a) Exploded-view schematic illustration of a skin-integrated wireless haptic interface with 32 independently controlled haptic actuators. b) Exploded-view schematic diagram of a haptic actuator. c) Schematic illustration of the wireless electronics and circuit; the main circuit components are labelled 1–6. d) Photograph of a skin-integrated wireless haptic interface based on voice-coil vibrotactile actuators under bending. e) A finite element analysis result of a skin-integrated wireless haptic interface under bending. The color represents the equivalent strain, and the insets show the areas with relatively high strain levels. f) Dynamic illustration of a skin-integrated haptic interface for a virtual reality application showing a ‘virtual touch process’ and ‘sense of virtual touch.’ A girl touches a screen that displays a video feed of her grandmother, who is wearing a skin-integrated wireless haptic interface on her hand and her arm (inset photograph). Reproduced with permission.^[51] Copyright 2019, Springer Nature.

Although most wearable or skin-integrated vibrotactile systems focus on the fingertips and, sometimes, the hands, an interesting opportunity is for advanced materials and device approaches that allow application across all regions of the human body. **Figure 5a–e** show an array of 32 electromagnetic actuators embedded in a soft elastomer layer, that operates wirelessly by harvesting radio-frequency power and communicating with controllers via near-field inductive

coupling.^[51] The actuators incorporate a mechanically compliant geometry, where freestanding magnets oscillate against the voice coils with induced AC signals **Figure 5b**. Here, a tightly wound thin copper coil (3 mm in inner diameter, 14 mm in outer diameter, 300 turns, 50 μm in wire diameter) attaches to a PDMS body (12 mm in inner diameter, 18 mm in outer diameter, 2.5 mm in thickness) to activate and move a permanent magnet (nickel-plated neodymium magnet; 8 mm in

diameter, 1.6 mm in thickness, 0.6 g in weight). The magnet attaches to a polyimide-based film (125 μm in thickness) in the shape of a circular ring with a semicircular slit in the middle. This structure acts as a cantilever for the magnet to maintain alignment to the center of the coil while freely vibrating. Each actuator weighs 1.4 g and operates with 1.75 mW input power (set at ≈ 5 mA in current) with resonant frequencies between 100 and 300 Hz. For maximum tactile sensation, the peak frequency (the highest vibration amplitude) is purposefully tuned, using theoretical models to guide design choices, to 200 Hz, achieved by either modifying the semicircular slit of the film or controlling the thickness and number of turns of the coil. The coils connect to a wireless power-harvester and communication circuit comprised of various system-on-chip ICs to communicate with an external control unit through near-field communication (NFC) protocols (Figure 5c). Stretchable serpentine copper structures (50–200 μm in width, 18 μm in thickness) form all electrical traces, including the power harvesting antenna, NFC antenna, and interconnects, which, when combined with an ultrathin layer of polyimide sheet (12.5 μm in thickness) as the circuit board, yield a mechanically compliant array layout. The actuators and electronic components bond to the circuit platform using low temperature solder joints. A soft encapsulation (2.5 mm in thickness) layer exploits a low modulus formulation of skin-colored PDMS (≈ 60 kPa) to yield a skin-compatible system with flexible, stretchable, and twistable mechanics (Figure 5d,e). A thin coating (≈ 0.1 mm) of an ultralow-modulus silicone (≈ 3.0 kPa) and a stretchable fabric substrate (Spandex) that incorporates strain-limiting mechanics prevent damage to the components. The naturally tacky surface facilitates reversible contact to the skin, with an adhesion energy of ≈ 90 N m^{-1} for hairless areas and ≈ 80 N m^{-1} for hairy areas. Various shapes of skin-integrated devices can be tailored for different body parts. For instance, devices with lateral geometries in butterfly (≈ 120 g in weight) and peanut (≈ 81 g in weight) shapes naturally fit on the back and upper limb, respectively.

Communication and power harvesting by NFC enables completely wireless, battery-free operation and control over the actuators, such that real-time manipulation and rapid, spatiotemporal commands are possible via a touch screen-enabled external controller (i.e., tablet computer) programmed with advanced graphical user interface (GUI) software. The GUI features frequency and amplitude tuning capabilities for the delivery of customized patterns of tactile sensations. Figure 5f illustrates the operation of the skin-integrated haptic interface for VR applications, where a baby touching on the screen remotely triggers a haptic sensation to a skin-integrated haptic interface worn by a person visible in the screen, in the form of a continuous wave of vibratory excitation in a spatiotemporal pattern of touch to match that of the baby's fingertips. Examples of potential uses range broadly from social media applications for virtual tactile interactions, prosthetic applications for reproducing the shape characteristics of objects, to gaming applications for activating various interaction modes during a game. Section 5 discusses these new opportunities, along with other possible uses that are unique to skin-integrated haptic interfaces.

4.3. Skin-Integrated Vibrotactile Interface Based on Piezoelectric Actuators

As mechanical interfaces, piezoelectric actuators are attractive for their lack of moving parts and their ability to be constructed in forms that are more compact and thinner than electromagnetic actuators, although most devices require substantial thicknesses to achieve meaningful displacements (see Section 3.2). As mentioned previously, an electrical input through metal plates of both sides of a piezoelectric layer generates controlled physical movements, with rapid displacements at small currents (a few micro amps) and relatively large voltages (a few hundred volts), as described in Section 3.2.3. Examples in Figure 6 describe the use of piezoelectric actuators for skin-integrated haptics and tactile feedback in VR/AR environments.

4.3.1. Designs and Applications for Skin-Integrated Piezoelectric Actuators

An example of a haptic feedback interface that uses PZT-based piezoelectric actuators attaches on the radial side of the fingertip.^[188] The purpose of this device is to enhance natural tactile sensations by generating a subsensory vibration on the surrounding mechanoreceptors, as a “sensorimotor enhancer.” A piezoelectric actuator based on PZT stack with a size (12.8 mm in length, 9 mm in width, 4.7 mm in thickness; Cedrat Technology) comparable to a fingertip mounts onto a modified latex cap with one side cut open. The user wears the cap with the actuator positioned to the radial side and the exposed (opened) region positioned to the palmar side of the fingertip. The piezoelectric actuator on the radial side leaves the palmar side exposed to allow direct skin interaction with objects. Upon a touch event, a simultaneous subsensory tactile feedback on the side of the fingertip enhances the sensation by intensifying the tactile receptors around the finger pulp, via a phenomenon known as stochastic resonance. Such enhancement can be valuable for tasks that require high-precision manual dexterity.

Studies with 11 participants show improvements for different tactile evaluations, including two-point discrimination tests, one-point touch tests, active sensory tests, and motor skill tests. The results of two-point discrimination tests indicate statistically significant differences for cases when the PZT actuator induces a vibrotactile sensation on the radial side of the fingertip, such that mean distances of discrimination decrease by $\approx 20\%$ for cases with vibration compared to without. A one-point touch test that involves a monofilament pressing onto the fingertips shows that threshold forces decrease by $\approx 20\%$ when the device delivers vibration. Results from a texture discrimination test that uses sandpapers with different grit sizes to measure correct rates exhibit an increased correct rate by up to $\approx 70\%$, when compared with a nonvibration case ($\approx 50\%$). A final motor skill test, which measures the minimal grasping force, shows that grasping an object with the radial vibration requires $\approx 90\%$ of the force that is needed for grasping without any vibration. The results in all cases indicate that different vibration amplitudes affect the sensory performance, and improvements occur with all the tested amplitude levels (50%, 75%, 100%, 125%, and 150% of perception threshold).

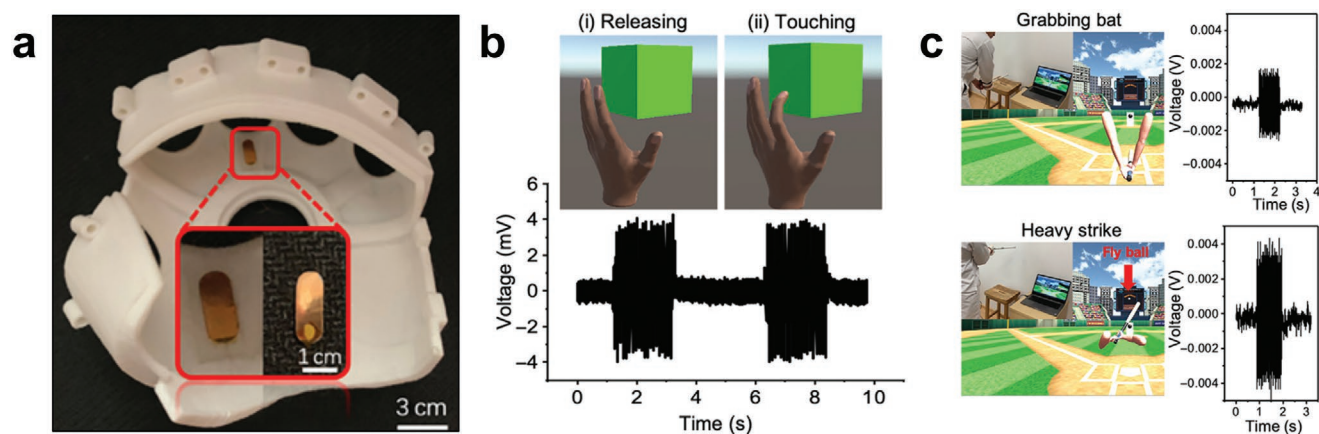


Figure 6. Skin-integrated piezoelectric vibratory actuators. a) Photograph of the bonded layers of a PZT vibratory stimulator and a PZT mechanical sensor placed inside a 3D-printed glove. The inset shows a magnified view. b) Schematic illustration (top) of real-time haptic feedback in response to interactive events (releasing and touching an object) in a virtual environment. Graph (bottom) of the vibration intensity generated by the stimulator. c) Schematic illustrations of a baseball gaming program (left) and plots of measured haptic stimulation intensities (right). Events such as grabbing a bat (top) and heavy striking (bottom) appear with screenshots of real-time demonstrations in the virtual environment (insets). Reproduced under the terms of the Creative Commons CC BY 4.0 License.^[33] Copyright 2020, the Authors. Published by The American Association for the Advancement of Science.

Figure 6a–c present an example of a virtual touch sensation using a haptic feedback interface based on a piezoelectric stimulator.^[33] Here, a piezoelectric sensor mounts on top of the stimulator for concurrent recording and stimulation. Specifically, the sensor converts mechanical signals induced by the stimulator into electrical signals, such that real-time stimulation can be visualized and analyzed. Fabrication begins with a polishing of a PZT ceramic surface (150 mm in length, 150 mm in width; Fuji Ceramics Inc.), followed by sputter-deposition of metal (Cr/Au, 20, 200 nm). This metalized side of the ceramic bonds to a copper foil using a conductive silver paste with vacuum annealing (3.5 h at 175 °C). A chemical mechanical polishing process applied to the opposing side of the ceramic thins the material to a thickness of 20 μm . Sputter-deposition of metal (Cr/Au, 20, 200 nm) defines the other contact. Laser cutting the film yields a single layer PZT (8 mm in length, 5 mm in width, 20 μm in thickness) coated with metal layers on both sides to form a PZT chip. Bonding two chips yields a dual-purpose device as an actuator and sensor. The actuator offers a resonant frequency of 270 Hz with a tunable intensity for driving voltages between 6 and 12 V. Psychophysical evaluations designate 6, 8, and 10 V inputs as light, medium, and strong vibratory forces on the palm of hand. Figure 6a shows the device mounted on the interior of a 3D-printed customized glove using silver paste to connect the wires on electrodes and polyimide tape to secure the device. Wearing this glove presses the PZT device directly on the skin.

Figure 6b presents a case of VR manipulation, where a visual reflection of a participant in the VR environment shows hand interactions, such as releasing and touching a virtual object. The bottom plots in Figure 6b illustrate signals from the sensor part of the system, as recordings of the intensity generated by the stimulation part of the device. In dynamic VR interactions, such as playing virtual baseball (Figure 6c), different vibrotactile intensities on gloves for different events, like virtually grabbing a baseball bat (top of Figure 6c) and striking heavily on the

ball (bottom of Figure 6c), provide immersive experiences to the user. Plots on the right of Figure 6c show that the haptic interface generates a significantly more intense vibration feedback when the user strikes heavily on the ball, compared to lightly grabbing a baseball bat.

An intimate physical contact of the actuators to the skin is essential. Traditional haptic gloves and exoskeletons employ straps, bands and related mechanisms with rigid structures around the hand for this purpose, but with drawbacks in added weight, impeded contact with the actuator, and constrained movements. A piezoelectric-based haptic interface focuses on mounting the actuators tightly on the fingertips using hook-and-loop fasteners along with a lightweight braking mechanism for kinesthetic feedback to minimize these limitations.^[189] Two piezoelectric vibrotactile actuators (10.5 mm in length, 3.8 mm in width, 2 mm in thickness; PiezoVibe, Murata) strap on the index finger and thumb. Each generates 1.2 G of vibratory acceleration (for a 20 g mass) at 240 Hz using 6 mW of power. An electrostatic brake, enabled by two metal strips to generate frictional force, creates kinesthetic feedback. The brake consists of thin flexible steel strips (18 cm in length, 1 cm in width, 100 μm in thickness), with one strip coated with a dielectric layer (polyimide, 13 μm in thickness), attached together to slide freely when no voltage is applied, but to generate 20 N of frictional force for a voltage of 1.5 kV at 20 Hz, as a result of electrostatic attraction. A combination of a piezoelectric actuator and electrostatic brake simultaneously provides haptic and kinesthetic feedback, respectively.

Capabilities in precise manipulation of virtual objects depend critically on tightly fitted, lightweight haptic interfaces. Participants engaged with such systems can manipulate virtual objects with precision and natural motions. Further work on materials may create opportunities for further reductions in size and increases in flexibility, as an improved skin interface and user experience.

5. Conclusion and Outlook

Systems for VR/AR represent one of the most exciting and fastest growing segments of modern technology, motivated by a compelling collection of application possibilities that span social media, entertainment, medicine, human–machine interfaces and training.^[190,191] Traditional work on haptic devices for such purposes focuses on engagement across the fingertips, often in the form of handheld devices, gloves or finger sleeves. A recent additional trend, highlighted by this review article, is toward large, skin-integrated platforms that can support interfaces to the skin at any location across the body. The vision is for full-body engagement as part of an immersive VR/AR system that qualitatively expands virtual experiences beyond visual and auditory inputs. This area offers tremendous opportunities for research in materials science and device engineering, not only in the development of advanced actuators, the main focus of this paper, but also across all other essential aspects of these systems, from integrated electronics, to data communication components, power supplies, and skin interfaces.

The engineering goal is for thin, skin-like platforms that interface with minimal mass loading or mechanical constraints on natural motions of the body and the skin, even at highly curved, sensitive regions, as a physically imperceptible active, high-speed, programmable technology, either as free-standing devices or as integrated parts of form-fitting garments. Successful outcomes have the potential to support virtual worlds, with essential features that cannot be reproduced through displays and speakers. This set of frontier possibilities is particularly important to continued improvements in technologies for VR/AR, simply because further enhancements of existing, highly developed video and audio systems will likely have only incremental significance on the user experience. Touch interfaces, by contrast, remain in a state of relative infancy, with potential for new ideas and research results to greatly and qualitatively improve the levels of immersion and functional options.

The consequences are interesting to contemplate. The most immediate observation is that capabilities for imitating real-world tactile cues will add meaning to VR/AR-enabled social connections and networking by adding physical touch—one of the deepest and most emotionally powerful means for interpersonal communication. The implications are significant in both professional and personal occasions, where physical engagements can catalyze and expand interactions and collaborations. For example, the ability to share, feel and manipulate virtual objects and to interact not only with the hands but other parts of the body will facilitate understanding of complex and sometimes subtle aspects of engagements that cannot be conveyed through sights and sounds alone.^[14,192,193] Other opportunities are in video games and entertainment, where vivid tactile sensations and physical interactions with characters or other users will create diverse means to shape experiences.^[194]

Virtual interactions that include tactile sensation will also promote medical treatments and facilitate the delivery of telemedicine, a trend with rapidly increasing recent momentum, due in part to a growing awareness created by the COVID-19 pandemic.^[195] The possibilities extend beyond traditional

forms of health care to emotional support for children or the elderly via comforting haptic feedback to encourage a sense of togetherness and security.^[37,196] Similar therapies can extend to a range of mental disorders, from posttraumatic stresses, to autism, mood instabilities, anxieties, and certain neurological disorders.^[19,197] Such psychotherapies are most effective when they include touch beyond the fingertips, to parts of the body that are most relevant for treatment purposes.

As an additional example of medical relevance, vibrohaptic systems can serve as control interfaces for robotic prosthetics, where they offer potential as a surrogate form of sensory engagement to replace capabilities lost through an amputation.^[17,22,198,199] Reported examples include sequences of haptic feedback signals to an unaffected region of the body as a means to control prosthetics with integrated sensors. The result can enable tasks that require delicate tactile information on objects in the environment, as discussed in Section 2.

Related applications also involve scenarios that benefit from information channels provided to the skin, as a complement to those supported by the eyes and ears. Examples are in the context of haptic navigation or warning systems and in advanced simulation training environments.^[200–202] As a case of the former, spatiotemporal patterns of tactile stimulation on different parts of the body can aid drivers or pilots, without distracting their view of the surroundings. An example of the latter is in virtual training for soldiers that includes various combat situations in simulated environments.

The vision for full-body haptic interfaces in these and many other scenarios will only be fulfilled if the supporting technology not only supports the necessary functionality but does so in a manner that imposes no burden on the user, with an imperceptible load on the body. These requirements represent daunting, but highly motivating, technical challenges that form the basis of a set of exciting topics for research and development in materials science and engineering. The actuators themselves appear to involve the most significant hurdles, but their integration into supporting technology systems is also critically important. Recent advances and synergistic continuing work in stretchable electronics and in energy harvesting and storage systems are essential in this context. Unusual schemes in wireless communication and power delivery, and in ultralow power electronic devices and computational systems, represent additional relevant areas of on-going research. Software control interfaces and sensors for closed-loop feedback to ensure reliable, safe, and reproducible sensations are also central to system operation. The underlying biology of haptic perception and the nature of skin-mediated device interfaces must be considered in any scheme. Interdisciplinary work in these contexts, geared toward a goal of skin-integrated haptic interfaces that can engage with all of the mechanoreceptors across all regions of the body, represents a powerful and broadly significant direction for research.

Acknowledgements

Y.H.J. and J.-H.K. contributed equally to this work. Y.H.J. was supported by the Basic Science Research Program (NRF-2018R1D1A1B07048988) through the National Research Foundation of Korea funded by the Ministry of Science, ICT and Future Planning.

Conflict of Interest

The authors declare no conflict of interest.

Keywords

electrotactile devices, flexible electronics, haptic interfaces, vibrotactile devices, virtual reality

Received: October 15, 2020

Revised: November 26, 2020

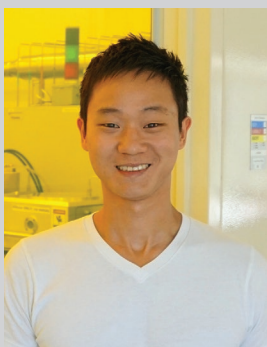
Published online: December 16, 2020

-
- [1] G. C. Burdea, P. Coiffet, *Virtual Reality Technology*, John Wiley & Sons, Hoboken, NJ **2003**.
- [2] D. A. Bowman, R. P. McMahan, *Computer* **2007**, *40*, 36.
- [3] S. D. Laycock, A. M. Day, *Comput. Graph. Forum* **2003**, *22*, 117.
- [4] P. B. Shull, D. D. Damian, *J. Neuroeng. Rehabil.* **2015**, *12*, 59.
- [5] H. Culbertson, S. B. Schorr, A. M. Okamura, *Annu. Rev. Control Rob. Auton. Syst.* **2018**, *1*, 385.
- [6] R. W. Lindeman, R. Page, Y. Yanagida, J. L. Sibert, presented at *VRST04: The ACM Symp. on Virtual Reality Software and Technology 2004*, Hong Kong, China, November **2004**.
- [7] K. A. Kaczmarek, J. G. Webster, P. Bach-y-Rita, W. J. Tompkins, *IEEE Trans. Biomed. Eng.* **1991**, *38*, 1.
- [8] P. Lopes, S. You, L.-P. Cheng, S. Marwecki, P. Baudisch, presented at *CHI'17: CHI Conf. on Human Factors in Computing Systems*, Denver, Colorado, USA **2017**.
- [9] S. Schätzle, T. Ende, T. Wüsthoff, C. Preusche, presented at *19th Int. Symp. in Robot and Human Interactive Communication*, Viareggio, Italy, September **2010**.
- [10] C. Pacchierotti, S. Sinclair, M. Solazzi, A. Frisoli, V. Hayward, D. Prattichizzo, *IEEE Trans. Haptics* **2017**, *10*, 580.
- [11] D. J. Lipomi, C. Dhong, C. W. Carpenter, N. B. Root, V. S. Ramachandran, *Adv. Funct. Mater.* **2020**, *30*, 1906850.
- [12] Y. Shao, V. Hayward, Y. Visell, *Proc. Natl. Acad. Sci. USA* **2016**, *113*, 4188.
- [13] S. Kim, K. Y. Kim, B. S. Soh, G. Yang, S. R. Kim, *IEEE Trans. Consum. Electron.* **2006**, *52*, 1340.
- [14] G. Huisman, *IEEE Trans. Haptics* **2017**, *10*, 391.
- [15] M. Zyda, *Computer* **2005**, *38*, 25.
- [16] Z. Pan, A. D. Cheok, H. Yang, J. Zhu, J. Shi, *Comput. Graph.* **2006**, *30*, 20.
- [17] S. Crea, B. B. Edin, K. Knaepen, R. Meeusen, N. Vitiello, *Phys. Ther.* **2017**, *97*, 198.
- [18] A. Turolla, M. Dam, L. Ventura, P. Tonin, M. Agostini, C. Zucconi, P. Kiper, A. Cagnin, L. Piron, *J. Neuroeng. Rehabil.* **2013**, *10*, 85.
- [19] C. Vaucelle, L. Bonanni, H. Ishii, presented at *CHI'09: CHI Conf. on Human Factors in Computing Systems*, Boston, MA, USA, April **2009**.
- [20] L. Haritaipan, M. Hayashi, C. Mougenot, *Adv. Hum. Comput. Interact.* **2018**, *2018*, 1.
- [21] M.-D. Tsai, M.-S. Hsieh, C.-H. Tsai, *Comput. Biol. Med.* **2007**, *37*, 1709.
- [22] P. D. Marasco, J. S. Hebert, J. W. Sensinger, C. E. Shell, J. S. Schofield, Z. C. Thumser, R. Nataraj, D. T. Beckler, M. R. Dawson, D. H. Blustein, S. Gill, B. D. Mensh, R. Granja-Vazquez, M. D. Newcomb, J. P. Carey, B. M. Orzell, *Sci. Transl. Med.* **2018**, *10*, eaao6990.
- [23] K. E. Laver, B. Lange, S. George, J. E. Deutsch, G. Saposnik, M. Crotty, *Cochrane Database Syst. Rev.* **2017**, *11*, CD008349.
- [24] L. Panait, E. Akkary, R. L. Bell, K. E. Roberts, S. J. Dudrick, A. J. Duffy, *J. Surg. Res.* **2009**, *156*, 312.
- [25] A. L. Butt, S. Kardong-Edgren, A. Ellertson, *Clin. Simul. Nurs.* **2018**, *16*, 25.
- [26] S. J. Robertson, J. Leonard, A. J. Chamberlain, *Aust. J. Dermatol.* **2020**, *51*, 220.
- [27] S. Scheggi, L. Meli, C. Pacchierotti, D. Prattichizzo, presented at *SIGGRAPH '15: Special Interest Group on Computer Graphics and Interactive Techniques Conf.*, Los Angeles, California, USA, July **2015**.
- [28] M. Shirali-Shahreza, S. Shirali-Shahreza, presented at *2009 11th Int. Conf. on Advanced Communication Technology*, February **2009**.
- [29] I. Choi, E. Ofek, H. Benko, M. Sinclair, C. Holz, presented at *CHI'18: CHI Conf. on Human Factors in Computing Systems*, Montreal, QC, Canada, April **2018**.
- [30] H. Benko, C. Holz, M. Sinclair, E. Ofek, presented at *UIST'16: The 29th Annual ACM Symp. on User Interface Software and Technology*, Tokyo, Japan, October **2016**.
- [31] C. V. Keef, L. V. Kayser, S. Tronboll, C. W. Carpenter, N. B. Root, M. FinnIII, T. F. O'Connor, S. N. Abuhamdi, D. M. Davies, R. Runser, Y. S. Meng, V. S. Ramachandran, D. J. Lipomi, *Adv. Intell. Syst.* **2020**, *2*, 2000018.
- [32] K. Minamizawa, S. Kamuro, S. Fukamachi, N. Kawakami, S. Tachi, presented at *SIGGRAPH '08: Special Interest Group on Computer Graphics and Interactive Techniques Conf.*, Los Angeles, CA, USA, August **2008**.
- [33] M. Zhu, Z. Sun, Z. Zhang, Q. Shi, T. He, H. Liu, T. Chen, C. Lee, *Sci. Adv.* **2020**, *6*, eaaz8693.
- [34] G. Yang, H. L. Ho, W. Chen, W. Lin, S. H. Yeo, M. S. Kurbanhusen, presented at *IEEE Conf. on Robotics, Automation and Mechatronics*, Singapore, Singapore, December **2004**.
- [35] I. Choi, H. Culbertson, M. R. Miller, A. Olwal, S. Follmer, presented at *UIST '17: The 30th Annual ACM Symp. on User Interface Software and Technology*, Québec City, QC, Canada **2017**.
- [36] I. Choi, E. W. Hawkes, D. L. Christensen, C. J. Ploch, S. Follmer, presented at *2016 IEEE/RSJ Int. Conf. on Intelligent Robots and Systems (IROS)*, Daejeon, South Korea, October **2016**.
- [37] L. Bonanni, C. Vaucelle, J. Lieberman, O. Zuckerman, presented at *CHI06: CHI 2006 Conf. on Human Factors in Computing Systems*, Montréal, QC, Canada, April **2006**.
- [38] Teslasuit. TESLASUIT is a full body haptic suit and training solution for physical VR experiences, <https://teslasuit.io/> (accessed: October 2020).
- [39] bHaptics. Tactsuit brings 'sense of touch' to virtual reality more closely than ever before imaginable, <https://www.bhaptics.com/> (accessed: October 2020).
- [40] D.-H. Kim, N. Lu, R. Ma, Y.-S. Kim, R.-H. Kim, S. Wang, J. Wu, S. M. Won, H. Tao, A. Islam, K. J. Yu, T.-i. Kim, R. Chowdhury, M. Ying, L. Xu, M. Li, H.-j. Chung, H. Keum, M. McCormick, P. Liu, Y.-W. Zhang, F. G. Omenetto, Y. Huang, T. Coleman, J. A. Rogers, *Science* **2011**, *333*, 838.
- [41] S. R. Krishnan, T. R. Ray, A. B. Ayer, Y. Ma, P. Gutruf, K. Lee, J. Y. Lee, C. Wei, X. Feng, B. Ng, Z. A. Abecassis, N. Murthy, I. Stankiewicz, J. Freudman, J. Stillman, N. Kim, G. Young, C. Goudeseune, J. Ciraldo, M. Tate, Y. Huang, M. Potts, J. A. Rogers, *Sci. Transl. Med.* **2018**, *10*, eaat8437.
- [42] H. U. Chung, B. H. Kim, J. Y. Lee, J. Lee, Z. Xie, E. M. Ibler, K. Lee, A. Banks, J. Y. Jeong, J. Kim, C. Ogle, D. Grande, Y. Yu, H. Jang, P. Assem, D. Ryu, J. W. Kwak, M. Namkoong, J. B. Park, Y. Lee, D. H. Kim, A. Ryu, J. Jeong, K. You, B. Ji, Z. Liu, Q. Huo, X. Feng, Y. Deng, Y. Xu, K.-I. Jang, J. Kim, Y. Zhang, R. Ghaffari, C. M. Rand, M. Schau, A. Hamvas, D. E. Weese-Mayer, Y. Huang, S. M. Lee, C. H. Lee, N. R. Shanbhag, A. S. Paller, S. Xu, J. A. Rogers, *Science* **2019**, *363*, eaau0780.

- [43] M. Kaltenbrunner, T. Sekitani, J. Reeder, T. Yokota, K. Kuribara, T. Tokuhara, M. Drack, R. Schwödiauer, I. Graz, S. Bauer-Gogonea, S. Bauer, T. Someya, *Nature* **2013**, 499, 458.
- [44] R. A. Nawrocki, N. Matsuhisa, T. Yokota, T. Someya, *Adv. Electron. Mater.* **2016**, 2, 1500452.
- [45] A. Miyamoto, S. Lee, N. F. Cooray, S. Lee, M. Mori, N. Matsuhisa, H. Jin, L. Yoda, T. Yokota, A. Itoh, M. Sekino, H. Kawasaki, T. Ebihara, M. Amagai, T. Someya, *Nat. Nanotechnol.* **2017**, 12, 907.
- [46] T. Shay, O. D. Velev, M. D. Dickey, *Soft Matter* **2018**, 14, 3296.
- [47] M. D. Dickey, *Adv. Mater.* **2017**, 29, 1606425.
- [48] S. Lee, Q. Shi, C. Lee, *APL Mater.* **2019**, 7, 031302.
- [49] J. Y. Oh, S. Rondeau-Gagné, Y.-C. Chiu, A. Chortos, F. Lissel, G.-J. N. Wang, B. C. Schroeder, T. Kurosawa, J. Lopez, T. Katsumata, J. Xu, C. Zhu, X. Gu, W.-G. Bae, Y. Kim, L. Jin, J. W. Chung, J. B.-H. Tok, Z. Bao, *Nature* **2016**, 539, 411.
- [50] S. Yao, Y. Zhu, *Adv. Mater.* **2015**, 27, 1480.
- [51] X. Yu, Z. Xie, Y. Yu, J. Lee, A. Vazquez-Guardado, H. Luan, J. Ruban, X. Ning, A. Akhtar, D. Li, B. Ji, Y. Liu, R. Sun, J. Cao, Q. Huo, Y. Zhong, C. Lee, S. Kim, P. Gutruf, C. Zhang, Y. Xue, Q. Guo, A. Chempakasseril, P. Tian, W. Lu, J. Jeong, Y. Yu, J. Cornman, C. Tan, B. Kim, K. Lee, X. Feng, Y. Huang, J. A. Rogers, *Nature* **2019**, 575, 473.
- [52] X. Wu, S. Kim, H. Zhu, C. Ji, M. G. Allen, *J. Microelectromech. Syst.* **2012**, 21, 908.
- [53] G. Ilkhani, E. Samur, presented at *2018 IEEE Haptics Symp. (HAPTICS)*, March **2018**.
- [54] H. Ishizuka, R. Hatada, C. Cortes, N. Miki, *Micromachines* **2018**, 9, 230.
- [55] S. Biswas, Y. Visell, *Adv. Mater. Technol.* **2019**, 4, 1900042.
- [56] A. B. Vallbo, R. S. Johansson, *Hum. Neurobiol.* **1984**, 3, 3.
- [57] P. R. Burgess, E. R. Perl, in *Somatosensory System*, Vol. 2 (Ed.: A. Iggo), Springer-Verlag, Berlin, Germany **1973**.
- [58] K. O. Johnson, *Curr. Opin. Neurol.* **2001**, 11, 455.
- [59] F. McGlone, J. Wessberg, H. Olausson, *Neuron* **2014**, 82, 737.
- [60] E. B. Goldstein, *Sensation and Perception*, Cengage Learning, Belmont, CA **2013**.
- [61] J. Sandby-Moller, T. Poulsen, H. C. Wulf, *Acta Derm.-Venereol.* **2003**, 83, 410.
- [62] R. Wong, S. Geyer, W. Weninger, J.-C. Guimberteau, J. K. Wong, *Exp. Dermatol.* **2016**, 25, 92.
- [63] P. Störchle, W. Müller, M. Sengeis, S. Lackner, S. Holasek, A. Fürhapter-Rieger, *Sci. Rep.* **2018**, 8, 16268.
- [64] S.-H. Woo, E. A. Lumpkin, A. Patapoutian, *Trends Cell Biol.* **2015**, 25, 74.
- [65] G. S. Harrington, J. Hunter Downs Iii, *Brain Res.* **2001**, 897, 188.
- [66] R. Ackerley, K. Saar, F. McGlone, H. Backlund Wasling, *Front. Behav. Neurosci.* **2014**, 8, 34.
- [67] S. Gilman, *J. Neurol. Neurosurg. Psychiatry* **2002**, 73, 473.
- [68] F. McGlone, D. Reilly, *Neurosci. Biobehav. Rev.* **2010**, 34, 148.
- [69] A. W. Roe, R. M. Friedman, L. M. Chen, in *Handbook of Neurochemistry and Molecular Neurobiology: Sensory Neurochemistry*, Vol. 3 (Eds: A. Lajtha, D. A. Johnson), Springer, Boston, MA **2007**.
- [70] H. Z. Tan, N. I. Durlach, C. M. Reed, W. M. Rabinowitz, *Percept. Psychophys.* **1999**, 61, 993.
- [71] V. Mountcastle, M. Steinmetz, R. Romo, *J. Neurosci.* **1990**, 10, 3032.
- [72] I. Birznieks, S. McIntyre, H. M. Nilsson, S. S. Nagi, V. G. Macefield, D. A. Mahns, R. M. Vickery, *eLife* **2019**, 8, e46510.
- [73] J. Ryu, J. Jung, G. Park, S. Choi, *Presence* **2010**, 19, 364.
- [74] I. Hwang, J. Seo, M. Kim, S. Choi, *IEEE Trans. Haptics* **2013**, 6, 352.
- [75] H.-Y. Yao, D. Grant, J. M. Cruz-Hernandez, *IEEE Trans. Haptics* **2010**, 3, 56.
- [76] F. Mancini, A. Bauleo, J. Cole, F. Lui, C. A. Porro, P. Haggard, G. D. Iannetti, *Ann. Neurol.* **2014**, 75, 917.
- [77] R. S. Johansson, Å. B. Vallbo, *Trends Neurosci.* **1983**, 6, 27.
- [78] C. Pasluosta, P. Kiele, T. Stieglitz, *Clin. Neurophysiol.* **2018**, 129, 851.
- [79] R. Ackerley, I. Carlsson, H. Wester, H. Olausson, H. Backlund Wasling, *Front. Behav. Neurosci.* **2014**, 8, 54.
- [80] W. Taube Navaraj, C. García Núñez, D. Shakhthivel, V. Vinciguerra, F. Labeau, D. H. Gregory, R. Dahiya, *Front. Neurosci.* **2017**, 11, 501.
- [81] A. Wilska, *Acta Physiol. Scand.* **1954**, 31, 285.
- [82] T. Schicke, B. Röder, *Proc. Natl. Acad. Sci. USA* **2006**, 103, 11808.
- [83] B. Delhay, V. Hayward, P. Lefèvre, J.-L. Thonnard, *Front. Behav. Neurosci.* **2012**, 6, 37.
- [84] L. R. Manfredi, A. T. Baker, D. O. Elias, J. F. Dammann, III, M. C. Zielinski, V. S. Polashock, S. J. Bensmaia, *PLoS One* **2012**, 7, e31203.
- [85] K. O. Sofia, L. Jones, *IEEE Trans. Haptics* **2013**, 6, 320.
- [86] S. Ryu, D. Pyo, S.-C. Lim, D.-S. Kwon, *Sci. Rep.* **2018**, 8, 4555.
- [87] R. M. Strong, D. E. Troxel, *IEEE Trans. Man-Mach. Syst.* **1970**, 11, 72.
- [88] K. A. Kaczmarek, M. E. Tyler, P. Bach-Y-Rita, presented at *16th Annual Int. Conf. of the IEEE Engineering in Medicine and Biology Society*, Baltimore, MD, USA, November **1994**.
- [89] W. Dong, Y. Wang, Y. Zhou, Y. Bai, Z. Ju, J. Guo, G. Gu, K. Bai, G. Ouyang, S. Chen, Q. Zhang, Y. Huang, *Int. J. Intell. Rob. Appl.* **2018**, 2, 313.
- [90] M. Štrbac, M. Belić, M. Isaković, V. Kojić, G. Bijelić, I. Popović, M. Radotić, S. Došen, M. Marković, D. Farina, T. Keller, *J. Neural Eng.* **2016**, 13, 046014.
- [91] A. Akhtar, J. Sombeck, B. Boyce, T. Bretl, *Sci. Rob.* **2018**, 3, eaap9770.
- [92] M. Štrbac, M. Isaković, J. Malešević, T. Keller, V. Ilić, N. Jorgovanović, S. Došen, presented at *2019 26th IEEE Int. Conf. on Electronics, Circuits and Systems (ICECS)*, November **2019**.
- [93] L. Seminara, H. Fares, M. Franceschi, M. Valle, M. Štrbac, D. Farina, S. Dosen, *IEEE Trans. Haptics* **2020**, 13, 393.
- [94] K. A. Kaczmarek, *IEEE Trans. Neural Syst. Rehabil. Eng.* **2000**, 8, 499.
- [95] B. Stephens-Fripp, V. Sencadas, R. Mutlu, G. Alici, *Front. Biotechnol.* **2018**, 6, 179.
- [96] T. Keller, A. Kuhn, *J. Automat. Contr.* **2008**, 18, 35.
- [97] M. Papiardanidou, S. Takamatsu, S. Rezaei-Mazinani, T. Lonjaret, A. Martin, E. Ismailova, *Adv. Healthcare Mater.* **2016**, 5, 2001.
- [98] B. Geng, W. Jensen, *J. Neuroeng. Rehabil.* **2014**, 11, 97.
- [99] M. D'Alonzo, S. Dosen, C. Cipriani, D. Farina, *IEEE Trans. Haptics* **2014**, 7, 181.
- [100] Precision Microdrives: Eccentric Rotating Mass Vibration Motors (ERMs), <https://www.precisionmicrodrives.com/vibration-motors/eccentric-rotating-mass-vibration-motors-erms/> (accessed: October 2020).
- [101] V. Yem, R. Okazaki, H. Kajimoto, presented at *2016 IEEE Haptics Symp. (HAPTICS)*, Philadelphia, PA, USA, April **2016**.
- [102] Jinlong Machinery and Electronics. Cylindrical & coin vibration motor used for haptic feedback, <https://www.vibration-motor.com/> (accessed: October 2020).
- [103] J. Martínez, A. García, M. Oliver, J. P. Molina, P. González, *IEEE Comput. Graph. Appl.* **2016**, 36, 42.
- [104] J. Martínez, A. S. García, M. Oliver, J. P. Molina, P. González, *Int. J. Hum.-Comput. Interact.* **2014**, 30, 855.
- [105] Precision Microdrives: Why is Vibration Amplitude in G, <https://www.precisionmicrodrives.com/content/why-is-vibration-amplitude-in-g/> (accessed: October 2020).
- [106] T. N. Do, H. Phan, T.-Q. Nguyen, Y. Visell, *Adv. Funct. Mater.* **2018**, 28, 1800244.
- [107] J. J. Zárate, G. Tosolini, S. Petroni, M. De Vittorio, H. Shea, *Sens. Actuator, A* **2015**, 234, 57.
- [108] Precision Microdrives: Linear Resonant Actuators – LRAs, <https://www.precisionmicrodrives.com/vibration-motors/linear-resonant-actuators-lras/> (accessed: October 2020).
- [109] I. Hwang, H. Lee, S. Choi, *IEEE Trans. Haptics* **2013**, 6, 340.

- [110] Texas Instruments. Haptic energy consumption—Application Report SLOA194, <https://www.ti.com/lit/pdf/sloa194> (accessed: October 2020).
- [111] H. Huang, T. Li, C. Antfolk, C. Enz, J. Justiz, V. M. Koch, presented at 2016 6th IEEE Int. Conf. on Biomedical Robotics and Biomechatronics (BioRob), June 2016.
- [112] Texas Instruments. Haptics: Solutions for ERM and LRA Actuators, <https://www.ti.com/lit/ml/sszb151/sszb151.pdf> (accessed: October 2020).
- [113] F. Carpi, D. De Rossi, R. Kornbluh, R. E. Pelrine, P. Sommer-Larsen, *Dielectric Elastomers as Electromechanical Transducers: Fundamentals, Materials, Devices, Models and Applications of an Emerging Electroactive Polymer Technology*, Elsevier, Oxford, UK 2011.
- [114] K. J. Kim, S. Tadokoro, *Electroactive Polymers for Robotic Applications: Artificial Muscles and Sensors*, Springer, New York, NY 2007.
- [115] J. D. W. Madden, N. A. Vandesteeg, P. A. Anquetil, P. G. A. Madden, A. Takshi, R. Z. Pytel, S. R. Lafontaine, P. A. Wieringa, I. W. Hunter, *IEEE J. Ocean. Eng.* **2004**, 29, 706.
- [116] P. Brochu, Q. Pei, *Macromol. Rapid Commun.* **2010**, 31, 10.
- [117] X. Yuan, S. Changgeng, G. Yan, Z. Zhenghong, *J. Phys.: Conf. Ser.* **2016**, 744, 012077.
- [118] B. Scrosati, *Applications of Electroactive Polymers*, Chapman & Hall, London, UK 1993.
- [119] J. Biggs, K. Danielmeier, J. Hitzbleck, J. Krause, T. Kridl, S. Nowak, E. Orselli, X. Quan, D. Schapeler, W. Sutherland, J. Wagner, *Angew. Chem., Int. Ed.* **2013**, 52, 9409.
- [120] Y. Bar-Cohen, presented at SPIE Smart Structures and Materials Symposium 2004, EAPAD Conf., San Diego, CA, USA, March 2004.
- [121] A. York, J. Dunn, S. Seelecke, *Smart Mater. Struct.* **2010**, 19, 094014.
- [122] R. Pelrine, R. Kornbluh, Q. Pei, J. Joseph, *Science* **2000**, 287, 836.
- [123] R. Pelrine, R. Kornbluh, J. Joseph, R. Heydt, Q. Pei, S. Chiba, *Mater. Sci. Eng., C* **2000**, 11, 89.
- [124] Y. Qiu, E. Zhang, R. Plamthottam, Q. Pei, *Acc. Chem. Res.* **2019**, 52, 316.
- [125] A. Poulin, S. Rosset, H. R. Shea, *Appl. Phys. Lett.* **2015**, 107, 244104.
- [126] I. M. Koo, K. Jung, J. C. Koo, J. Nam, Y. K. Lee, H. R. Choi, *IEEE Trans. Rob.* **2008**, 24, 549.
- [127] S. Vishniakou, B. W. Lewis, X. Niu, A. Kargar, K. Sun, M. Kalajian, N. Park, M. Yang, Y. Jing, P. Brochu, Z. Sun, C. Li, T. Nguyen, Q. Pei, D. Wang, *Sci. Rep.* **2013**, 3, 2521.
- [128] S. Mun, S. Yun, S. Nam, S. K. Park, S. Park, B. J. Park, J. M. Lim, K. Kyung, *IEEE Trans. Haptics* **2018**, 11, 15.
- [129] L. Maffli, S. Rosset, H. R. Shea, *Smart Mater. Struct.* **2013**, 22, 104013.
- [130] E. Acome, S. K. Mitchell, T. G. Morrissey, M. B. Emmett, C. Benjamin, M. King, M. Radakovitz, C. Keplinger, *Science* **2018**, 359, 61.
- [131] P. Rothemunda, S. Kirkmana, C. Keplinger, *Proc. Natl. Acad. Sci., USA* **2020**, 117, 16207.
- [132] N. Kellarisa, V. G. Venkata, P. Rothemund, C. Keplinger, *Extreme Mech. Lett.* **2019**, 29, 100449.
- [133] E. Leroy, R. Hinchet, H. Shea, *Adv. Mater.* **2020**, 32, 2002564.
- [134] R. E. Pelrine, R. D. Kornbluh, J. P. Joseph, *Sens. Actuator, A* **1998**, 64, 77.
- [135] L. Yiming, R. Kai Liang, H. F. Hofmann, Z. Qiming, *IEEE Trans. Ultrason. Ferroelectr. Freq. Control* **2005**, 52, 2411.
- [136] Q. M. Zhang, V. Bharti, X. Zhao, *Science* **1998**, 280, 2101.
- [137] C. Ramstein, A. Liaukeviciute, *Inf. Disp.* **2014**, 30, 36.
- [138] T. Safwat, R. Tosto, M. D. Grissom, C. D. Rahn, presented at ASME 2016 Int. Design Engineering Technical Conf. and Computers and Information in Engineering Conf., August 2016.
- [139] A. O'Halloran, F. O'Malley, P. McHugh, *J. Appl. Phys.* **2008**, 104, 071101.
- [140] S. Nemat-Nasser, S. Zamani, presented at SPIE Smart Structures and Materials Symposium 2003, EAPAD Conf., San Diego, CA, USA, March 2003.
- [141] M. Hao, Y. Wang, Z. Zhu, Q. He, D. Zhu, M. Luo, *Front. Rob. AI* **2019**, 6, 129.
- [142] J. Kim, S. D. Deshpande, S. Yun, Q. Li, *Polym. J.* **2006**, 38, 659.
- [143] K. Uchino, *Piezoelectric Actuators and Ultrasonic Motors*, Kluwer Academic Publishers, Norwell, MA 1996.
- [144] Q. Guo, G. Z. Cao, I. Y. Shen, *J. Vib. Acoust.* **2013**, 135, 011003.
- [145] Q. M. Zhang, Z. Jianzhong, *IEEE Trans. Ultrason. Ferroelectr. Freq. Control* **1999**, 46, 1518.
- [146] Q. Q. Zhang, S. J. Gross, S. Tadigadapa, T. N. Jackson, F. T. Djuth, S. Trolier-McKinstry, *Sens. Actuator, A* **2003**, 105, 91.
- [147] R. Zhang, B. Jiang, W. Cao, *J. Appl. Phys.* **2001**, 90, 3471.
- [148] I. Alexandru Ivan, M. Rakotondrabe, J. Agnus, R. Bourquin, N. Chaillet, P. Lutz, J.-C. Poncot, R. Duffait, O. Bauer, *Rev. Adv. Mater. Sci.* **2010**, 24, 1.
- [149] D. Berlincourt, H. Jaffe, *Phys. Rev.* **1958**, 111, 143.
- [150] G. M. Sessler, *J. Acoust. Soc. Am.* **1981**, 70, 1596.
- [151] I. Katsouras, K. Asadi, M. Li, T. B. van Driel, K. S. Kjær, D. Zhao, T. Lenz, Y. Gu, P. W. M. Blom, D. Damjanovic, M. M. Nielsen, D. M. de Leeuw, *Nat. Mater.* **2016**, 15, 78.
- [152] L. Ruan, X. Yao, Y. Chang, L. Zhou, G. Qin, X. Zhang, *Polymers* **2018**, 10, 228.
- [153] L. Li, M. Zhang, M. Rong, W. Ruan, *RSC Adv.* **2014**, 4, 3938.
- [154] R. E. Roy, S. Bhuvaneshwari, K. P. Vijayalakshmi, R. Dimple, P. B. Soumyamol, R. S. N. Rajeev, *J. Polym. Sci., B: Polym. Phys.* **2019**, 57, 40.
- [155] M. Fortunato, D. Cavallini, G. De Bellis, F. Marra, A. Tamburrano, F. Sarto, M. S. Sarto, *Polymers* **2019**, 11, 1096.
- [156] W. Ma, J. Zhang, S. Chen, X. Wang, *Appl. Surf. Sci.* **2008**, 254, 5635.
- [157] C. Dagdeviren, P. Joe, O. L. Tuzman, K.-I. Park, K. J. Lee, Y. Shi, Y. Huang, J. A. Rogers, *Extreme Mech. Lett.* **2016**, 9, 269.
- [158] N. Kar Lai, C. Helen Lai Wa, C. Chung Loong, *IEEE Trans. Ultrason. Ferroelectr. Freq. Control* **2000**, 47, 1308.
- [159] N. R. Alluri, B. Saravanakumar, S.-J. Kim, *ACS Appl. Mater. Interfaces* **2015**, 7, 9831.
- [160] D.-S. Choi, S.-Y. Kim, *Sensors* **2019**, 19, 3490.
- [161] S. H. Yoon, S. Ma, W. S. Lee, S. Thakurdesai, D. Sun, F. P. Ribeiro, J. D. Holbery, presented at UIST '19: The 32nd Annual ACM Symp. on User Interface Software and Technology, New Orleans, LA, USA, 2019.
- [162] C. Dagdeviren, Y. Shi, P. Joe, R. Ghaffari, G. Balooch, K. Usgaonkar, O. Gur, P. L. Tran, J. R. Crosby, M. Meyer, Y. Su, R. Chad Webb, A. S. Tedesco, M. J. Slepian, Y. Huang, J. A. Rogers, *Nat. Mater.* **2015**, 14, 728.
- [163] C. Dagdeviren, Y. Su, P. Joe, R. Yona, Y. Liu, Y.-S. Kim, Y. Huang, A. R. Damadoran, J. Xia, L. W. Martin, Y. Huang, J. A. Rogers, *Nat. Commun.* **2014**, 5, 4496.
- [164] K. Uchino, *MRS Bull.* **1993**, 18, 42.
- [165] A. Dogan, K. Uchino, R. E. Newnham, *IEEE Trans. Ultrason. Ferroelectr. Freq. Control* **1997**, 44, 597.
- [166] K. Uchino, S. Takahashi, *Curr. Opin. Solid State Mater. Sci.* **1996**, 1, 698.
- [167] K. Lubitz, H. Hellebrand, presented at 1990 IEEE 7th Int. Symp. on Applications of Ferroelectrics, Urbana-Champaign, IL, USA, June 1990.
- [168] W. Qing-Ming, D. Xiao-Hong, X. Baomin, L. E. Cross, *IEEE Trans. Ultrason. Ferroelectr. Freq. Control* **1999**, 46, 638.
- [169] TDK Corporation. PiezoHapt™ Actuators, https://product.tdk.com/info/en/products/sw_piezo/haptic/piezohapt/index.html (accessed: October 2020).
- [170] TDK Corporation. PowerHap™ Actuators, https://product.tdk.com/info/en/products/sw_piezo/haptic/powerhap/index.html (accessed: October 2020).

- [171] H. A. Sonar, J. Paik, *Front. Rob. AI* **2016**, 2, 38.
- [172] S. S. Robinson, K. W. O'Brien, H. Zhao, B. N. Peele, C. M. Larson, B. C. Mac Murray, I. M. Van Meerbeek, S. N. Dunham, R. F. Shepherd, *Extreme Mech. Lett.* **2015**, 5, 47.
- [173] C. W. Carpenter, M. G. Malinao, T. A. Rafeedi, D. Rodriguez, S. T. M. Tan, N. B. Root, K. Skelil, J. Ramirez, B. Polat, S. E. Root, V. S. Ramachandran, D. J. Lipomi, *Adv. Mater. Technol.* **2020**, 5, 1901119.
- [174] J. J. Huaroto, E. Suarez, H. I. Krebs, P. D. Marasco, E. A. Vela, *IEEE Rob. Autom. Lett.* **2019**, 4, 17.
- [175] E. Suarez, J. J. Huaroto, A. A. Reymundo, D. Holland, C. Walsh, E. Vela, presented at *2018 IEEE Int. Conf. on Robotics and Automation (ICRA)*, Brisbane, QLD, Australia, May **2018**.
- [176] A. P. G. H. A. Sonar, S. P. Lacour, J. Paik, *Soft Robot* **2020**, 7, 22.
- [177] M. Perović, M. Stevanović, T. Jevtić, M. Štrbac, G. Bijelić, Č. Vučetić, L. Popović-Maneski, D. B. Popović, *J. Autom. Contr.* **2013**, 21, 13.
- [178] M. Franceschi, L. Seminara, S. Dosen, M. Strbac, M. Valle, D. Farina, *IEEE Trans. Haptics* **2017**, 10, 162.
- [179] G. Chai, X. Sui, S. Li, L. He, N. Lan, *J. Neural Eng.* **2015**, 12, 066002.
- [180] Z. Turi, G. G. Ambrus, K.-A. Ho, T. Sengupta, W. Paulus, A. Antal, *Brain Stimul.* **2014**, 7, 460.
- [181] G. Kantor, G. Alon, H. S. Ho, *Phys. Ther.* **1994**, 74, 951.
- [182] A. Akhtar, B. Boyce, T. Bretl, presented at *2014 IEEE Haptics Symp. (HAPTICS)*, February **2014**.
- [183] B. Xu, A. Akhtar, Y. Liu, H. Chen, W.-H. Yeo, S. I. Park, B. Boyce, H. Kim, J. Yu, H.-Y. Lai, S. Jung, Y. Zhou, J. Kim, S. Cho, Y. Huang, T. Bretl, J. A. Rogers, *Adv. Mater.* **2016**, 28, 4462.
- [184] M. Ying, A. P. Bonifas, N. Lu, Y. Su, R. Li, H. Cheng, A. Ameen, Y. Huang, J. A. Rogers, *Nanotechnology* **2012**, 23, 344004.
- [185] A. Withana, D. Groeger, J. Steimle, presented at *UIST '18: The 31st Annual ACM Symp. on User Interface Software and Technology*, Berlin, Germany, October **2018**.
- [186] L. M. Ferrari, K. Keller, B. Burtcher, F. Greco, *Multifunct. Mater.* **2020**, 3, 032003.
- [187] O. Ozioko, P. Karipoth, M. Hersh, R. Dahiya, *IEEE Trans. Neural Syst. Rehabil. Eng.* **2020**, 28, 1344.
- [188] Y. Kurita, M. Shinohara, J. Ueda, *IEEE Trans. Hum. Mach. Syst.* **2013**, 43, 333.
- [189] R. Hinchet, V. Vechev, H. Shea, O. Hilliges, presented at *UIST '18: The 31st Annual ACM Symp. on User Interface Software and Technology*, Berlin, Germany, October **2018**.
- [190] F. Wen, Z. Sun, T. He, Q. Shi, M. Zhu, Z. Zhang, L. Li, T. Zhang, C. Lee, *Adv. Sci.* **2020**, 7, 2000261.
- [191] Z. Zhang, T. He, M. Zhu, Z. Sun, Q. Shi, J. Zhu, B. Dong, M. R. Yuce, C. Lee, *npj Flex. Electron.* **2020**, 4, 29.
- [192] A. Haans, W. Ijsselsteijn, *Virtual Reality* **2006**, 9, 149.
- [193] A. Haans, W. A. Ijsselsteijn, *IEEE Trans. Haptics* **2009**, 2, 136.
- [194] M. Orozco, J. Silva, A. El Saddik, E. Petriu, in *Haptics Rendering and Applications* (Ed.: A. E. Saddik), InTech, Rijeka, Croatia **2012**, Ch. 11.
- [195] J. E. Hollander, B. G. Carr, *N. Engl. J. Med.* **2020**, 382, 1679.
- [196] J. K. S. Teh, A. D. Cheok, Y. Choi, C. L. Fernando, R. L. Peiris, O. N. N. Fernando, presented at *IDC '09: The 8th International Conf. on Interactive Design and Children*, Como, Italy, June **2009**.
- [197] A. Rizzo, A. Hartholt, M. Grimani, A. Leeds, M. Liewer, *Computer* **2014**, 47, 31.
- [198] J. K. S. Teh, Z. Tsai, J. T. K. V. Koh, A. D. Cheok, presented at *2012 IEEE Haptics Symp. (HAPTICS)*, Vancouver, BC, Canada, March **2012**.
- [199] B. Stephens-Fripp, G. Alici, R. Mutlu, *IEEE Access* **2018**, 6, 6878.
- [200] F. Kiss, R. Boldt, B. Pflöging, S. Schneegass, presented at *CHI '18: CHI Conf. on Human Factors in Computing Systems*, Montreal, QC, Canada, April **2018**.
- [201] J. B. F. Van Erp, H. A. H. C. Van Veen, *Transp. Res., Part F: Traffic Psychol. Behav.* **2004**, 7, 247.
- [202] M. L. McLaughlin, G. Sukhatme, J. Hespanha, *Touch in Virtual Environments: Haptics and the Design of Interactive Systems*, Prentice Hall PTR, Upper Saddle River, NJ **2001**.



Ye Hwan Jung obtained B.S. degree (2011) from the University of Illinois at Urbana-Champaign, and M.S. degree (2015) and Ph.D. degree (2017) from the University of Wisconsin-Madison, all in Electrical Engineering. He is currently a postdoctoral research associate at Northwestern University. His research interests lie in developing unconventional microfabrication techniques using thin film materials to create high-performance flexible and stretchable devices with applications for bioelectronics.



Jae Hwan Kim obtained his B.S. (2015) from the Department of Materials Science and Engineering and his M.S. (2018) from the Department of Electrical and Computer Engineering at the University of Illinois at Urbana-Champaign. Under the supervision of Prof. John A. Rogers, his research focus is on battery-free, wearable electronics for wireless biomedical applications.



John A. Rogers obtained B.A. and B.S. degrees in Chemistry and in Physics from the University of Texas Austin, in 1989. From MIT, he received S.M. degrees in Physics and in Chemistry in 1992 and his Ph.D. degree in Physical Chemistry in 1995. In 2016, he joined Northwestern University as the Louis Simpson and Kimberly Querrey Professor of Materials Science and Engineering, Biomedical Engineering, and Medicine, with affiliate appointments in Mechanical Engineering, Electrical and Computer Engineering, and Chemistry, where he is also Director of the recently endowed Querrey-Simpson Institute for Bioelectronics.